



# Surface evolution and wind effects during a cyclonic eddy splitting event in the Balearic Sea

Sebastien Donnet<sup>1</sup>, Helga S. Huntley<sup>2</sup>, Maristella Berta<sup>3</sup>, Luca Centurioni<sup>4</sup>, Leo Middleton<sup>5</sup>, Tamay Özgökmen<sup>6</sup>, Pierre-Marie Poulain<sup>7</sup>, and Annalisa Griffa<sup>3</sup>

<sup>1</sup>Conservatoire des Arts et Métiers Intechmer, Cherbourg-en-Cotentin, France

<sup>2</sup>Department of Mathematics, Rowan University, Glassboro, NJ, USA

<sup>3</sup>Consiglio Nazionale delle Ricerche - Istituto di Scienze Marine, Lerici, Italy

<sup>4</sup>Scripps Institution of Oceanography, University of California San Diego, La Jolla, CA, USA

<sup>5</sup>Woods Hole Oceanographic Institution, Woods Hole, MA, USA

<sup>6</sup>Rosenstiel School of Marine and Atmospheric Sciences, University of Miami, Miami, FL, USA

<sup>7</sup>NATO-STO-CMRE, La Spezia, Italy

**Correspondence:** Maristella Berta ([maristella.bera@sp.ismar.cnr.it](mailto:maristella.bera@sp.ismar.cnr.it))

**Abstract.** During the period of 23 - 28 February 2022, a cyclonic eddy in the Balearic Sea was observed to split into two smaller eddies. Serendipitously, a wealth of data was collected of the event, including satellite chlorophyll maps, Lagrangian drifters at several depths, hydrographic sections intersecting the splitting eddy, and wind speed and direction. Sufficiently many drifters were in the area to estimate kinematic properties (divergence, vorticity, and strain rate) from clusters along the edge of the eddy before and during the elongation period that led to the splitting. The vertical velocity  $w$  can be computed from colocated divergence values from surface drifters (CARTHE and CODE, within the top meter) and near-surface drifters (SVP, at 15m depth). Together, the observations delineate the process of eddy elongation, leading to vorticity and strain-rate intensification on February 25, followed by the collapse of the ridge in the center of the eddy and the emergence of smaller eddies on February 26, terminating with the splitting into submesoscale cyclones on February 28. The consecutive daily hydrography and drifter observations supplement the remotely sensed descriptive view of the eddy splitting process. In particular, they confirm dominant internal dynamics, consistent with isopycnal doming, but also point to a role played by the winds, which shifted from predominantly southwesterly to predominantly northeasterly and strengthened significantly before weakening again in the area of interest during the eddy splitting period. Nonlinear Ekman pumping  $W_{Eknl}$  is estimated from the wind data and drifter-derived vorticities to capture the contribution of the wind effects to the patterns of up- and downwelling accompanying the eddy splitting. The  $W_{Eknl}$  patterns are consistent with the drifter-based  $w$  and divergence estimates. Moreover, the nonlinear Ekman pumping is found to be of the same order of magnitude as (though generally less than)  $w$ , suggesting that the wind likely plays a role in the observed surface processes.

## 1 Introduction

Ocean eddies are ubiquitous and are subject to complex dynamics (Fu et al., 2015; Petersen et al., 2013; McWilliams, 1985). Much of what is known about them has been informed by remote sensing. Global satellite observations have permitted quantita-



tive characterizations of eddies, at least at the mesoscale and the upper end of the submesoscale, compatible with the resolution of the observations (Martínez-Moreno et al., 2021; Fu et al., 2015). Both globally (Chelton et al., 2011) and in regional seas like the Mediterranean Sea (Escudier et al., 2016; Mkhinini et al., 2014), large cyclonic eddies have been found to be on average shorter-lived than anticyclones. This is consistent with theoretical results that cyclones are more prone to weakening and splitting (Nof, 1990, 1991; Arai and Yamagata, 1994; Polvani et al., 1994; Graves et al., 2006).

Numerical model studies (Amores et al., 2018) have suggested that at the present spatial resolution of gridded altimetry products such as AVISO/CMEMS, which are frequently used as the basis for eddy counts and analyses, only approximately 16% of eddies in the Mediterranean Sea can be detected and that the unresolved features can significantly alias the larger structures. Moreover, Stegner et al. (2021) have shown that cyclone detection in the Mediterranean is significantly less reliable than anticyclone detection, because large cyclones tend to split into small submesoscale cyclones characterized by rapid dynamics that cannot be resolved by the altimetry data. These smaller cyclones are, thus, likely to be generally undercounted and yet important to the ocean dynamics. Indeed, sunglitter reflections observed from space are consistent with their pervasiveness (Munk et al., 2000). Cyclones are also known to be associated with nutrient upwelling due to isopycnal doming, potentially triggering biological blooms (Cao et al., 2024). The process of cyclone deformation and splitting typically involves various scales and could play an important role at the submesoscale, concurring at the forward energy cascade which dissipates energy from larger to smaller scales in the ocean (McWilliams, 2019). Moreover, cyclone splitting, characterized by enhanced vertical exchanges along the water column, could influence the subduction of surface waters rich in carbon to the interior ocean, fundamental process in the biological carbon pump (Resplandy et al., 2019).

To properly capture the distribution and dynamics of submesoscale eddies, satellite observations must be supplemented with in situ data. During a recent experiment in the Balearic Sea (Northwest Mediterranean Sea), as part of the CALYPSO project (Mahadevan et al., 2020), a comprehensive suite of observations was collected during a cyclonic eddy splitting event, including satellite imagery, ship-based Eulerian measurements of the hydrography, and Lagrangian data from drifter releases at multiple depths within the top 15 m. The eddy was originally identified in remotely sensed chlorophyll-A maps, then targeted for in situ measurements. Its initial radius was  $\approx 10$  km (Fig. 1), with a shallow mixed layer of  $\approx 20$  m (Middleton et al., submitted 2024, M24 in the following). Over the course of five days, it split into two smaller cyclones with radii less than  $\approx 5$  km, i.e., much smaller than the typical Rossby radius in the area  $\approx 10$  km (Escudier et al., 2016). The recent comparison by M24 of the subsurface characteristics of this eddy breakup to an idealized model without external shear or wind stress determined that the splitting can be explained by the eddy shape, size, and intensity alone. Their analysis also suggested intense and localized subduction of surface waters associated with the event.

While wind forcing is, thus, not needed for eddies to split, this particular eddy splitting was accompanied by significant wind events. This raises the question of its role at least in the surface dynamics and whether wind can enhance (or diminish) the subduction associated with the event and the corresponding transport of biological tracers like chlorophyll and pollutants like microplastics from the mixed layer to greater depths. The focus here is on the evolution within the surface layer and its interaction with the wind, as illuminated by the drifter observations with drogues centered at 0.4 m and 0.75 m for the surface and at 15 m depth for the near-surface. The dense drifter observations allow an estimation of kinematic properties (KP), i.e.,



of vorticity, strain rate, and divergence. These, when obtained from nearly co-located drifters at multiple depths, in turn, can be used to derive estimates of vertical velocities. Wind intensification effects due to non-linear Ekman pumping on divergence and vertical velocity in the sea surface layer can thus be captured.

An overview of the observed eddy splitting event and the physical processes likely associated with it is given in Section 2.

60 Sections 3 and 4 detail the observations and analysis methods, respectively. Section 5 provides a detailed description of the eddy evolution based on drifter and hydrography data, followed by the analysis of wind effects and their contribution to the observed dynamics. The paper wraps up with a discussion and conclusions in Section 6.

## 2 Background

### 2.1 The near-surface dynamics of eddy splitting

65 The eddy splitting event examined here was observed northwest of the island of Mallorca in the Balearic Sea, in the Northwestern Mediterranean Sea (Fig. 1, bottom panel). The area is characterized by intense mesoscale and submesoscale eddy activity, fed by instabilities of the Northern Boundary Current and the Balearic Front (Pinot et al., 1994; Ruiz et al., 2009). The mixed layer depth at the time was relatively shallow, approximately 20 m, as deduced from the Brunt-Vaisala frequency calculated from in situ hydrography (Fig. SM1; see also M24). The eddy could be identified in satellite chlorophyll concentration maps as  
70 early as 17 February 2022 and was targeted for intense sampling starting 23 February, shortly before it began elongating (Fig. 1, left panel). The wind in the area was approximately from the southwest, roughly parallel to the eddy axis, with an intensification lasting about one day (Fig. 2). The variational mapping analysis by M24 of the subsurface data obtained for the area shows an elliptic cyclone with doming isopycnals characterized by subsurface vorticity reaching values of the order of the inertial frequency  $f$ . The smoothed divergence field, averaged over the top 60 m and 37 hours, exhibits a quadrupole pattern (M24's  
75 Fig. 4), consistent with cyclogeostrophic effects that in highly curved flows can alter the geostrophic balance. In essence, as the flow approaches the narrow end of an elliptical eddy, it accelerates due to centrifugal forces creating convergence, while it diverges after passing the tip.

Over the next few days, the elongation is observed to increase, as the eddy strains (Fig. 1 top, central panel. Refer also to the animation SM2). Idealized modeling, reported by M24, suggests that the convergence areas of the quadrupole caused  
80 vortex stretching in two patches, elevating the positive vorticity and creating two smaller eddies. By 26 February, the center of the ridge collapses while the smaller eddies intensify and become fully separated by 28 February (Fig. 1 top, right panel). Meanwhile, the wind, which was weak throughout 24 February, strengthens swiftly, likely due to a Tramontane event starting on 25 February and lasting until 27 February, with prevalent direction from the northwest (Fig. 2).

Thus, the eddy experiences both internal instabilities triggered by the eddy shape and its high intensity (high Rossby number)  
85 and significant wind forcing, especially during the period 25 – 27 February. These processes interact nonlinearly. The vertical vorticity  $\zeta$  in the eddy modifies the ‘effective’ Coriolis parameter  $f_{\text{eff}} = f + \zeta/2$  and thereby influences Ekman transport, potentially leading to nonlinear Ekman pumping (Stern, 1965; Niiler, 1969; Hart, 2000; Wenegrat and Thomas, 2017; McGillicuddy et al., 2007; Mahadevan et al., 2008). This, in turn, can modify the pressure field and therefore the eddy structure. The vor-



ticity gradients associated with the edges of eddies can also modify the local nonlinear inertial oscillations (NIO), leading to surface convergence and divergence in the surface layer with associated pumping effects (Perkins, 1976; Kunze, 1985; Elipot et al., 2010; Asselin and Young, 2020; Esposito et al., 2023). Moreover, Ekman and NIO effects can interact during periods of transient forcing, through energy transfer from high to low frequencies (Chen et al., 2021).

Ekman transport requires a period of at least two to three days under quasi-steady forcing to be fully established, although the time scale depends on several parameters including the strength of the wind forcing and eddy viscosity (Kirincich and Barth, 2009; Berta et al., 2018). On shorter time scales, only a fraction of the full Ekman transport is found in the surface layer. The event investigated here is characterized by high variability in the wind forcing (Fig. 2). The evolution and splitting of the eddy occurs over five days, while the wind variability has a scale of one to three days. This complicates the analysis. We anticipate that the interaction between eddy and wind effects is less straightforward than in the classical quasi-steady picture (Wenegrat and Thomas, 2017).

In order to identify the wind effects, we propose the following strategy. The densely distributed drifter data, from repeated launches in the first meter and at 15 m, are used to compute the kinematic properties (KPs), namely vorticity, strain rate, and divergence. Where drifters at the two depths are co-located, it is also possible to estimate the vertical velocity  $w$  (Esposito et al., 2023). This allows us to describe the surface layer evolution for 23 – 28 February, with a temporal resolution of 1 day. Wind effects are expected to be particularly evident in the divergence field, since it is directly influenced by wind (Chen et al., 2021), while vorticity and strain rate are mostly dominated by mesoscale and submesoscale dynamics (Esposito et al., 2021). While the high temporal variability in the wind inhibits the establishment of a fully developed Ekman transport and associated pumping, the tendency toward that state is expected to influence the surface layer. We therefore estimate the theoretical Ekman transport and pumping during the main wind episodes, following the theory briefly reviewed in Section 2.2, and relate these estimates to the observed divergence.

As mentioned above, NIOs can also impact the divergence field in the vicinity of the eddy. The daily averaging will dampen their signal, but cannot fully eliminate it, in part because the inertial period (approximately 19 h) differs from the 24 h averaging time, but more fundamentally because of the nature of Lagrangian sampling, which is by definition not fixed in space. The quickly evolving eddy field necessarily makes the interpretation of the NIO effects on divergence more qualitative than is possible in the context of a quasi-steady jet (Esposito et al., 2023). We have to rely on the detection of smaller scale patterns and deviations with respect to the Ekman tendency.

## 2.2 Ekman transport and pumping

According to linear Ekman theory (Cushman-Roisin and Beckers, 2011), non-zero wind stress curl induces positive or negative Ekman pumping, referring to the upwelling and downwelling responses, respectively, of the Ekman layer. Assuming an eddy viscosity of  $0.05 \text{ m}^2/\text{s}$ , a typical Ekman depth at the relevant latitudes is roughly 30 m. Recall that for weak surface ocean currents, the wind stress exerted on the ocean surface is given by

$$\tau_{wind} = \rho_a C_D \mathbf{u}_{wind} |\mathbf{u}_{wind}| \quad (1)$$





where  $C_D$  is a drag coefficient,  $\rho_a$  is the air density,  $|\mathbf{u}_{wind}|$  is the wind speed (at 10 m). Non-zero wind stress induces Ekman transport  $\mathbf{M}_{wind} = \langle U_{wind}, V_{wind} \rangle$ , integrated over the depth of the surface Ekman layer, that is directed perpendicular to the stress and rotated to the right in the northern hemisphere, with magnitude

$$125 \quad |\mathbf{M}_{wind}| = \frac{|\boldsymbol{\tau}_{wind}|}{\rho_0 f} \quad (2)$$

where  $\rho_0$  is the mean water density in the Ekman layer. Non-zero divergence in the Ekman transport gives rise to Ekman pumping, with a vertical velocity proportional to the curl of the wind stress:

$$w_{wind} = \nabla \cdot \mathbf{M}_{wind} = \frac{\nabla \cdot (\boldsymbol{\tau}_{wind} \times \mathbf{k})}{\rho_0 f} = \frac{\mathbf{k} \cdot \nabla \times \boldsymbol{\tau}_{wind}}{\rho_0 f}. \quad (3)$$

Here  $\mathbf{k}$  is the upward unit vector.

130 Nonlinear effects modify these formulas (Stern, 1965; Wenegrat and Thomas, 2017). When ocean currents  $\mathbf{u} = \langle u, v \rangle$  have significant magnitude relative to the wind, the stress  $\boldsymbol{\tau}$  acting on the ocean surface depends on the relative velocity  $\mathbf{u}_{rel} = \mathbf{u}_{wind} - \mathbf{u}$ :

$$\boldsymbol{\tau} = \rho_a C_D \mathbf{u}_{rel} |\mathbf{u}_{rel}| \quad (4)$$

and the associated Ekman transport and pumping velocity are modified by the vorticity  $\zeta$  in the Ekman layer:

$$135 \quad |\mathbf{M}_{Ekn}| = \frac{|\boldsymbol{\tau}|}{\rho_0 (f + \zeta)}, \quad (5)$$

$$w_{Ekn} = \nabla \cdot \frac{\boldsymbol{\tau} \times \mathbf{k}}{\rho_0 (f + \zeta)}. \quad (6)$$

The total Ekman pumping velocity  $w_{Ekn}$  can be decomposed into two parts, one depending only on the vorticity and the other also involving the vorticity gradient (Song et al., 2020):

$$w_{Ekn} = w_\zeta + w_{\nabla\zeta} = \frac{\mathbf{k} \cdot \nabla \times \boldsymbol{\tau}}{\rho_0 (f + \zeta)} + \frac{\mathbf{k} \cdot (\boldsymbol{\tau} \times \nabla \zeta)}{\rho_0 (f + \zeta)^2} = \frac{1}{\rho_0 (f + \zeta)} \left( \frac{\partial \tau^y}{\partial x} - \frac{\partial \tau^x}{\partial y} \right) + \frac{1}{\rho_0 (f + \zeta)^2} \left( \tau^x \frac{\partial \zeta}{\partial y} - \tau^y \frac{\partial \zeta}{\partial x} \right), \quad (7)$$

140 where  $\boldsymbol{\tau} = \langle \tau^x, \tau^y \rangle$  and we have assumed an  $f$ -plane approximation. In order to concentrate on the contribution to  $w_{Ekn}$  due to ocean currents (Gaube et al., 2015), and in agreement with the observations, we assume a clear scale separation between the wind velocity, that provides a smooth large scale background, and the ocean currents, characterized by mesoscale and submesoscale eddies with significant local vorticity  $\zeta$ , while neglecting the nonlinear dependence of the stress on the relative velocity.

145 The two terms in  $w_{Ekn}$  describe two different mechanisms. The first one,  $w_\zeta$ , (Dewar and Flierl, 1987; McGillicuddy et al., 2007) results from the curl of the relative surface stress  $\boldsymbol{\tau}$  that, according to the assumptions stated above, is dominated by the wind velocity, scaled by the ‘effective’ Coriolis parameter  $f + \zeta$ , which is modified by the local surface vorticity  $\zeta$ . Within a mesoscale eddy, the resulting Ekman pumping is expected to have opposite sign with respect to the local vorticity, resulting in upwelling in an anticyclonic eddy and downwelling in a cyclonic one. Gaube et al. (2015) evaluated  $w_\zeta$  for an isolated  
150 idealized cyclone, finding downwelling in the core, with elongation in the direction of the wind.



The second term,  $w_{\nabla\zeta}$ , (McGillicuddy et al., 2007) results from the vorticity gradients, divided by the square of the ‘effective’ Coriolis parameter. Conceptually, within our assumptions, this term is due to the fact that Ekman transport  $\mathbf{M}_{E_{knl}}$  (eq. 5) decreases with increasing magnitude of positive  $\zeta$ , inducing downwelling (and upwelling for decreasing positive  $\zeta$ ), while the opposite is true for negative  $\zeta$ . This mechanism leads to the formation of dipoles within the core of an isolated eddy (Gaubert et al., 2015), as shown in the cartoon in Fig. 3. For a cyclone, downwelling is expected to occur on the left side of the eddy core with respect to the wind (in the northern hemisphere) and upwelling on the right side. This is because the transport  $\mathbf{M}_{E_{knl}}$  is directed to the right of the wind, and therefore enters the eddy from its left side with respect to the wind, leading to downwelling in order to adjust for increasing  $\zeta$  and decreasing transport. The opposite occurs on the other side of the eddy, where  $\zeta$  decreases and transport increases. For anticyclones the dipole structure is inverted with respect to the wind.

## 3 Observations

### 3.1 Drifter Data

The analysis here is based on the surface and near-surface observations of drifter trajectories, complemented by ancillary data from satellites and ship-board instruments. Several significant drifter deployments were carried out during the CALYPSO cruise in February/March 2022 to sample the near-surface currents in specific submesoscale features with high horizontal resolution (order of 1 km). Three types of drifters were released in or near the cyclonic eddy considered in this paper: CARTHE (Consortium for Advanced Research on the Transport of Hydrocarbon in the Environment) drifters, drogued at 0.4 m (Novelli et al., 2017; D’Asaro et al., 2018), CODE (Coastal Ocean Dynamics Experiment) drifters, drogued at 0.75 m (Davis, 1985; Poulain, 1999), and SVP (Surface Velocity Program) drifters, drogued at 15 m (Niiler, 2001; Lumpkin and Pazos, 2007; Centurioni, 2018). CARTHE and CODE drifters have been found to measure currents representative of the top meter of the water column with accuracy of a few cm/s, assuming limited wind or wave induced slippage and Stokes drift (Poulain et al., 2022), and will be treated collectively as “surface” drifters (following, e.g., Esposito et al., 2021; Tarry et al., 2021) with a reference depth of 0 m, referred to below as CaC drifters. The SVP drifters have been shown to follow the sub-surface currents within 1 cm/s in winds up to 10 m/s (Niiler et al., 1995). GPS positions were sampled every 10 min via GlobalStar satellites for CARTHE and CODE drifters and every 5 min via satellite Iridium telemetry for SVP drifters. The drifter positions were processed with standard methods for quality control (Menna et al., 2017) and interpolated to uniform 5-min intervals starting at the top of the hour. Velocities were estimated by central finite differencing of these positions. Finally, position and velocity data were low-pass filtered with a Hamming window of 30 min. Drifter data in the area of interest on three days during the analysis is shown as cyan (CARTHE and CODE) and blue (SVP) curves in Fig. 1.



### 3.2 Wind Data

180 To evaluate the wind effects on the eddy, we use the ERA5 reanalysis 10-m winds from the European Centre for Medium-Range Weather Forecasts distributed by the Copernicus Climate Change Service (Hersbach et al., 2023). The data are available hourly on a  $0.25^\circ \times 0.25^\circ$  grid. Here we use daily averages derived from the hourly archive; see vector field in Fig. 1.

For local validation of the reanalysis winds, we compare wind speed and wind stress to in situ observations obtained from the standard shipboard instruments during the CALYPSO 2022 cruise. Two ships participated in the experiment, the *R/V Pourquoi Pas?* and the *R/V Pelagia*. Both were equipped with anemometers recording data at a nominal frequency of 1 Hz. These  
185 were mounted at 30 m and 27 m, respectively. Resulting wind measurements were converted to 10-m winds using the power law from Johnson (1999). Wind stress magnitude is computed from the measured wind speeds using the bulk aerodynamic formula assuming negligible surface ocean currents compared to the wind  $|\tau| = c_D \rho_a |\mathbf{u}_{wind}|^2$ , where  $c_D = 0.0015$  is the drag coefficient,  $\rho_a = 1.2 \text{ kg/m}^3$  is an average air density, and  $\mathbf{u}_{wind}$  is the wind velocity at 10 m. Ship tracks and time series  
190 of wind speed and stress magnitude are shown in Fig. 2.

### 3.3 Ancillary Data

Context is provided by ancillary data collected during the cruise. The eddy was first identified for intense sampling in satellite ocean color imagery, as illustrated in Fig. 1. The phytoplankton chlorophyll concentrations shown are a product of the Copernicus Marine Environment Monitoring Service (CMEMS) that combines data from multiple satellites (SeaWiFS, MODIS,  
195 MERIS, VIIRS-SNPP, VIIRS-JPSS1, OLCI-S3A, and OLCI-S3B) (CMEMS, 2022; Volpe et al., 2019). Temporal resolution is daily, and spatial resolution is 1 km.

Hydrographic information is obtained from EcoCTD profiles taken along multiple sections during the experiment (Mahadevan and D'Asaro, 2024). The EcoCTD includes sensors for conductivity, temperature, and density (RBR Concerto CTD), a chlorophyll fluorometer and backscatter meter (WETLabs BB2F), and an oxygen sensor (JFE Advantech Rinko), all mounted  
200 in a weighted aluminum housing and tow-yoed manually from the stern of the *R/V Pourquoi Pas?* with an Oceanscience UCTD winch (Dever et al., 2020). Typical operation of the EcoCTD was to make one profile to 250 m every 5 – 6 minutes at a vessel speed of 6 knots. Its data was calibrated against the CTD rosette. While multiple sections were sampled that intersected with the eddy, here we focus on the single temperature and salinity section for each day that is most nearly colocated with the drifter observations in time and space, shown as red lines in Fig. 1.

## 205 4 Method

### 4.1 Kinematic Properties Estimates from Drifters

A variety of methods exist for extracting KPs from drifter observations (Molinari and Kirwan Jr., 1975; Okubo et al., 1976; Kawai, 1985; Berta et al., 2015; Gonçalves et al., 2019). Here we obtain area-averaged KP estimates from drifter triplets, following Method I from Molinari and Kirwan Jr. (1975). Divergence  $\delta$ , averaged over time and the area of a triangle defined



210 by a drifter triplet, is computed from the change in that area over 15-minute intervals:

$$\delta = \frac{\log(A(t + \Delta t)) - \log(A(t))}{\Delta t}. \quad (8)$$

Vorticity  $\zeta$ , normal strain rate  $N$ , and shear strain rate  $S$  are computed similarly, from rotated velocity components, following Saucier (1955). The latter two quantities are combined in a total strain rate  $\alpha = \sqrt{N^2 + S^2}$ .

To eliminate those estimates that are subject to large errors due to the geometry of the drifter triplets, we filter out groups  
215 that do not satisfy the threshold  $\Lambda > 0.2$  on the scaled triangle aspect ratio  $\Lambda = 12\sqrt{3}A/P^2$ , where  $A$  is the area and  $P$  the  
perimeter of the triangle (Huntley et al., 2022). Area-averaged KPs are known to be scale-dependent (Berta et al., 2020). So,  
only triplets with the distance between each pair of drifters (side length of the resulting triangle) between 1 and 10 km are  
used. To ensure independent sampling, triplets sharing more than one drifter with an already listed triplet are eliminated. The  
resulting estimates are associated with the corresponding triplet centers of mass, then binned in  $2 \text{ km} \times 2 \text{ km}$  boxes and  
220 averaged over bins and time for daily gridded maps.

Drifter clusters can also be used to derive pointwise KP estimates by using least-squares fits (Molinari and Kirwan Jr., 1975;  
Okubo et al., 1976). Pointwise-estimates tend to have larger extremes than averages. So, a direct one-to-one comparison with  
area-averaged estimates is not advisable. However, as a form of validation, we carried out a qualitative comparison between  
the triplet-based area-averaged and cluster-based pointwise estimates of vorticity from CARTHE/CODE drifters with spatial  
225 scales of 2 – 4 km. (This is a subset of the estimates entering the bins used in the rest of the paper). For the least-squares fits,  
clusters were formed consisting of 6 or more drifters, all at most 4 km apart from the centroid, with an aspect ratio equal or  
larger than 0.1, defined as the ratio of the smaller to larger eigenvalue of the position covariance matrix (Essink et al., 2022).  
To ensure independent sampling, redundant clusters, i.e. those with overlapping drifter membership of more than 75%, were  
removed. Fig. 4 shows the vorticity scaled by the Coriolis parameter  $f = 9.4717 \times 10^{-5} \text{ s}^{-1}$  derived from triplets (triangles)  
230 and from clusters (circles) for 23 February 2022. The results demonstrate consistency between the two very different methods,  
in line with method comparisons reported elsewhere (e.g. Berta et al. (2020)).

## 4.2 Vertical Velocity Estimates from Drifters

When horizontally colocated divergence estimates are available at different depths, vertical velocities can be approximated from  
the continuity equation  $u_x + v_y + w_z = 0$ , where  $u$ ,  $v$ , and  $w$  are the eastward, northward, and upward velocity components,  
235 respectively. It follows that

$$w(-h) = w(h_{ref}) + \int_{-h}^{h_{ref}} (u_x + v_y) dz. \quad (9)$$

To obtain a vertical velocity estimate, both the vertical velocity at a reference depth  $h_{ref}$  and a vertical profile of horizontal  
divergence are needed. The reference depth is typically either taken to be the surface, where vertical velocities approximately  
vanish (Tarry et al., 2022), or a deep “depth of no motion” (Lodise et al., 2020). Here, we follow Tarry et al. (2022) and use the  
240 surface at  $z = 0$ . In lieu of a continuous vertical profile of the horizontal divergence, we rely on a first-order approximation, in-



terpolating linearly between the two known depths (Esposito et al., 2023). Thus, if we denote the known horizontal divergences at depths  $-h_0$  and  $-h_1$  as  $\delta_0$  and  $\delta_1$ , then

$$w(-h) = \frac{2(\delta_0 h_1 - \delta_1 h_0)h - (\delta_0 - \delta_1)h^2}{2(h_1 - h_0)}. \quad (10)$$

For our sampling depths of  $h_0 = 0$  m and  $h_1 = 15$  m, the vertical velocity at  $h = 15$  m is then given by

$$w(-15) = 15 \frac{(\delta_0 + \delta_1)}{2}. \quad (11)$$

## 5 Results

### 5.1 Daily surface eddy evolution

In this section, we describe the evolution of the eddy day-by-day during the splitting period, 23 – 28 February, skipping 24 and 27 February when insufficient data are available for a meaningful analysis. KP values shown are normalized by the local Coriolis parameter  $f$ , taken to be  $9.57 \times 10^{-5}$ , computed for a latitude of  $40.5^\circ\text{N}$ . Subsurface drifters are more sparse and primarily add insight to the eddy splitting analysis on 23 February, when the co-location of the two drifter datasets allows direct computation of the vertical velocity  $w$ . While available, we therefore do not show SVP results for other dates. The selected ecoCTD sections provide a three-dimensional context.

#### 5.1.1 23 February

During 23 February (Fig. 5), the surface CaC drifters sample mostly the southern flank of the cyclonic eddy, characterized by northeastward flow, and the northern edge of an adjacent anticyclonic structure, indicated by the curvature in the trajectories (Fig. 5a). Velocities along the edge of the cyclone reach a maximum value of 0.94 m/s. The strong velocities sampled by the drifters straddle the boundary between the cyclone and its adjacent anticyclonic region, with vorticity  $\zeta$  (Fig. 5b) showing high positive values, exceeding  $\zeta = f$ , to the north, characterizing the cyclone core, and negative, less extreme values to the south. This is consistent with the UCTD section (Fig. 5e), showing the characteristic isopycnal doming within the cyclone, coincident with positive drifter-derived  $\zeta$  (Fig. 5f) and a pronounced front separating the region with negative  $\zeta$ . The strain rate (Fig. 5d) is especially pronounced in the northern part of the coverage, corresponding to the area of high positive  $\zeta$  within the cyclone. As anticipated, divergence  $\delta$  (Fig. 5c) shows a more complex pattern, that at first glance is not straightforwardly consistent with the eddy structure. It shows a prominent positive pattern, with values reaching  $f$ , roughly located at the boundary between positive and negative  $\zeta$ , indicating upwelling, sandwiched between two smaller negative bands, suggesting downwelling. Along the section (Fig. 5f),  $\delta$  is negative within the eddy and slightly positive at the front. Overall, this detailed view is more complicated than the smoothed quadrupole pattern described by M24 based on variational mapping. The values of both vorticity and divergence found from the drifter analysis are significantly higher than reported by M24, likely due to the smoothing in the latter.



270 The 15-m SVP drifters (Fig. 6) show similar patterns (Fig. 5), although the KP values are slightly attenuated, as can be expected (Esposito et al., 2021). Vertical velocities  $w$ , computed for the co-located bins (Fig. 6e), are mostly positive (upwelling), reaching values  $\mathcal{O}(50 - 60 \text{ m/day})$ , except for a small negative band to the north. The pattern mirrors the surface  $\delta$  (Fig. 5c) in the overlapping region, confirming that surface divergence is a good indicator of upwelling and downwelling.

The presence of the anticyclonic structure to the southeast of the eddy and the high strain rate at the border of the cyclone  
275 suggest that large-scale straining could have played a role at least in the initial phase of the eddy elongation (even though M24 showed it is not strictly necessary to explain the eddy evolution). The day of 23 February was also characterized by increased winds, that could have played a role in the observed upwelling and divergence patterns. This point will be discussed in Section 5.2.

### 5.1.2 25 February

280 For 25 February (Fig. 7), no satellite chlorophyll data are available to place the in situ observations into a larger context. However, the surface trajectories appear to sample the core of the cyclone, showing a recirculating elongated structure and reaching maximum velocity values of  $0.75 \text{ m/s}$  (Fig. 7a). The drifters capture the strong positive vorticity  $\zeta$  (Fig. 7b), exceeding  $2f$ , in the center (consistent with M24's subsurface analysis), coincident with the maximum strain rate (Fig. 7d), which also reaches values of  $2f$ . The cyclone strengthening is accompanied by the strong isopycnal outcropping in the UCTD section  
285 (Fig. 7e), whereby the highest  $\zeta$  values occur at the edge of the front, as expected (Fig. 7f). The values of  $\delta$  along the section (Fig. 7f) are consistent with upwelling within the cyclone and downwelling at the southern front. The overall divergence pattern (Fig. 7c) shows mostly positive values northwest of the central core and negative values to the southeast, but exhibits additional complexity, with high small-scale variability.

The observed surface vorticity evolution agrees with M24's idealized model of an unforced eddy splitting event, and the  
290 high observed strain rates developing within the eddy are suggestive of ellipticity processes making the eddy prone to splitting. However, the drifters do not replicate a quadrupole pattern for the divergence. Especially in the southern part of the eddy the alternating signs of divergence (Fig. 7f) are the opposite of what would be expected for cyclo-geostrophic effects. This is additional evidence of wind effects.

### 5.1.3 26 February

295 During 26 February (Fig. 8), the surface drifters are mostly following a southwestward current, aligned with the wind, with maximum velocities of  $0.79 \text{ m/s}$  (Fig. 8a). They do not show recirculation at the scale of the main eddy, but do capture recirculation in two smaller submesoscale eddies that have formed at the northern and southern extremes of their sampling region. The collapse of the original eddy structure can also be detected in the isopycnals in Fig. 8e, that have drastically deepened and flattened relative to the previous day. The vorticity (Fig. 8b) within the filament connecting the two smaller  
300 eddies is positive and strong, exceeding  $\zeta = 2f$ , with very high strain rate (Fig. 8d) in the same area. Positive vorticity maxima also occur within the two spun off eddies. The divergence (Fig. 8c) is mostly negative within the main filament and consistent





with the observed downwelling associated with the collapsing of the isopycnals (Fig. 7e vs. Fig. 8e), with a drop of about 40 m in one day. Within the eddies the  $\delta$  structure is more complex with alternating positive and negative values.

As in the previous days, the overall evolution of the eddy in terms of vorticity and strain rate is compatible with a cyclo-geostrophic explanation (M24). The surface drifters show the corresponding central downwelling area, but, again, suggest that more complex dynamics are responsible for the high variability within the smaller eddies, including significant upwelling areas.

#### 5.1.4 28 February

By 28 February (Fig. 9), the original eddy structure has completely split into smaller cyclones. There are now three submesoscale eddies, with a tenuous connection between them, traced out by the surface drifters, which reach maximum velocity values of 0.70 m/s (Fig. 9a). All the eddies are characterized by intense cyclonic vorticity reaching  $\zeta = 2f$  (Fig. 9b), with patches of high strain rate (Fig. 9d). Divergence (Fig. 9c) again shows high small-scale variability, although it is mostly positive, indicative of upwelling, inside the southernmost eddy. Upwelling is also consistent with the newly developing doming of the isopycnals seen in the section through this eddy (Fig. 9e). High positive vorticity coincides with the doming (Fig. 9f).

#### 5.1.5 Synopsis

The drifters illustrate the process of eddy elongation, and permit the quantification of the strong vorticity intensification and internal strain rate occurring on 25 February, followed by the collapse of the eddy center and the emergence of smaller eddies on 26 February, and terminating with the splitting into three submesoscale cyclones on 28 February. The overall picture of vorticity and strain rate evolution is consistent with the cyclo-geostrophic explanation proposed by M24 based on the analysis of subsurface data and model results. This suggests that the process at the surface is also mostly dominated by internal dynamics, even though the drifters also provide evidence of a possible contribution of large-scale strain rate in the initial eddy elongation. The divergence patterns, on the other hand, are different, with the drifters showing bands of alternating divergence and convergence, indicative of upwelling and downwelling. The wind, which was particularly strong on 26 February, at the height of the splitting, is likely to have impacted the surface layer. Its contributions to the observed divergence patterns and related vertical velocities are explored next.

### 5.2 Wind effects

Our investigation into possible wind effects considers contributions from nonlinear Ekman pumping  $w_{E_{knl}}$  (see Section 2.2) and NIOs (see Section 2.1), concentrating on the days of significant wind forcing, i.e., 23 and 25 – 27 February. As discussed in Section 2.1, even though the time scales are such that  $w_{E_{knl}}$  is not expected to be fully established, the tendency toward  $w_{E_{knl}}$  is expected to leave a signature in the observed patterns.

Recall that there are two components of nonlinear Ekman pumping (eq. 7):  $w_{\zeta}$  and  $w_{\nabla\zeta}$ . For an isolated cyclone (Gaube et al., 2015),  $w_{\zeta}$  is expected to lead to downwelling in the core, with elongation in the direction of the wind. Here, the observations



(Section 5.1) clearly show the presence of a cyclonic eddy but are too sparse to delineate its complete spatial structure, let alone its surroundings. Consequently, we can only provide a qualitative description of the expected contribution of  $w_{\zeta}$ . The observed  
335 pattern of isopycnal downwelling and increasing ellipticity observed during the eddy evolution (Section 5.1) is consistent with a tendency toward downwelling and eddy elongation along the wind direction. Its relevance, though, depends on the value of the expected  $w_{\zeta}$ . An order of magnitude estimate, using  $|\mathbf{u}_{wind}| \approx 7 - 10$  m/sec,  $|\mathbf{u}| \approx 0.10 - 0.5$  m/sec,  $|\zeta| \approx 1 - 2f$  yields a corresponding range for  $w_{\zeta}$  of  $\approx 1 - 1.5$  m/day, which is more than an order of magnitude smaller than the  $w$  derived from the drifter divergence calculations (Fig. 6) and implied by the observed isopycnal drop of more than 40 m on 26 February (Fig. 8).  
340 We therefore conclude that, even though  $w_{\zeta}$  may contribute to the eddy evolution and its vertical velocity, its contribution is secondary and cannot explain the observed evolution.

The second term  $w_{\nabla\zeta}$  depends on the vorticity gradient and on wind direction. As for  $w_{\zeta}$ , we cannot provide a complete direct assessment of  $w_{\nabla\zeta}$  since our measurements are spatially limited. Some considerations and estimates, though, can be provided combining the information from the wind data during the two events and the observed vorticity  $\zeta$ . As a first step,  
345 we again perform an order of magnitude analysis, assuming the same ranges for  $|\mathbf{u}_{wind}| \approx 7 - 10$  m/sec and  $|\mathbf{u}| \approx 0.10 - 0.5$  m/sec, and for the vorticity gradients  $\nabla\zeta \approx \Delta\zeta/\Delta r \approx f/(5 - 10)$  km, where  $r$  is the relevant spatial scale. The corresponding  $w_{\nabla\zeta}$  is estimated in the range  $5 - 20$  m/day, which is comparable to the order of magnitude of the measured  $w$ .

A more precise estimate of  $w_{\nabla\zeta}$  is possible where there is enough data coverage. The linear Ekman transport  $\mathbf{M}_{wind}$  (eq. 2) is shown in Fig. 10 (top panels) for 23, 25, and 26 February, respectively, with the nonlinear transport  $|\mathbf{M}_{Ekn}|$  (eq. 5)  
350 superimposed wherever vorticity  $\zeta$  is available from drifters (Figs. 5, 7, 8). As expected,  $|\mathbf{M}_{Ekn}|$  is lower than the background in the cyclonic eddy (positive  $\zeta$ ), but higher in the anticyclonic areas (negative  $\zeta$ ).

A corresponding estimate of  $w_{\nabla\zeta}$  for 23 February (Fig. 10d) shows a prominent upwelling pattern, reaching values of  $w_{\nabla\zeta} \approx 20$  m/day in the transition area between positive and negative  $\zeta$  (Fig. 5b). In this region, the transport  $|\mathbf{M}_{Ekn}|$  increases significantly in the direction of propagation of transport (Fig. 10a). Conceptually, this corresponds to the upwelling on the side  
355 of the cyclone to the right of the wind (Fig. 3). Some downwelling can be seen at the southern edge of the available data, where negative vorticity starts to decrease. The vertical velocity  $w$  computed from the drifters for the same day (Fig. 6e) shows a similar predominantly upwelling pattern in the same area. The surface divergence (Fig. 5b) is also consistently positive there, indicating upwelling.

A quantitative comparison between the estimated  $w_{\nabla\zeta}$  and the actual  $w$  from the drifters is shown in Fig. 11. In grid cells  
360 where both values are available, the ratio  $w/w_{\nabla\zeta}$  is computed (panel (a)). It is almost entirely positive, reflecting that both estimates consistently show upwelling in this area. The few values greater than 1 indicate that a downwelling tendency from another source is softening the wind effect. Fig. 11b compares the histograms of the full vertical velocity and the Ekman pumping component. It shows that  $w$  reaches values of  $50 - 60$  m/day, while  $w_{\nabla\zeta}$  has a more peaked distribution, reaching only 20 m/day.

365 For 25 February, the background transport direction (northwestward, Fig. 10b) and the cyclone vorticity structure (Fig. 7b) characterized by a maximum in the core of the eddy lead us to expect upwelling to occur north of the maximum and downwelling south of the maximum, consistent with Fig. 3. Because of the reduced drifter coverage on this day that limits the gradient



calculation and because of the orientation of the vorticity maximum, the computation of  $w_{\nabla\zeta}$  is limited to the downwelling side in the northwestern portion of the eddy and to the upwelling side in the southeastern portion (Fig. 10e), with maximum  
370  $w_{\nabla\zeta} \approx 10$  m/day. For this day, the drifter-based  $w$  estimates have very limited coverage, but the surface divergence  $\delta$  (Fig. 7c) exhibits a pattern of positive and negative  $\delta$  to the northwest and to the southeast of the maximum  $\zeta$ , respectively, suggestive of upwelling and downwelling as in Fig. 10e.

Finally, for 26 February, the  $w_{\nabla\zeta}$  estimates (Fig. 10f) are mostly confined within the southernmost emerging eddy structure, since the elongated filament is too narrow to compute significant cross gradients. Due to the alternating negative and positive  
375 vorticity within the structure (Fig. 8b), and the transport direction (Fig. 10c), a pattern of positive and negative  $w_{\nabla\zeta}$  to the east and west, respectively, emerges (Fig. 10f). For this day, no  $w$  estimates are available from drifters for comparison, but the  $\delta$  estimates (Fig. 8c) show a consistent pattern of positive and negative divergence in the same area. We note that the main convergence/downwelling area observed in the central structure between the two eddies, and consistent with the isopycnal drop (Fig. 7e to Fig. 8e), does not have an obvious signature in terms of wind effects and is likely to be due to internal dynamics, as  
380 suggested by the subsurface analysis of M24.

In addition to nonlinear Ekman pumping effects, the wind is also likely to induce NIOs that can affect the divergence and  $w$  distributions. As discussed in Section 2, we are not in a position to provide a quantitative estimate of these effects since we have only a partial picture of the eddy vorticity structure, which is moreover rapidly evolving, as is the wind. On the other hand, some general observations should be considered. For instance, in the presence of a vorticity maximum, we can expect  
385 that the NIOs tend to create two bands of opposite  $\delta$  on either sides of the maximum (Esposito et al., 2023), with alternating sign in time at the inertial period (approximately 19 h). For 25 February, a maximum  $\zeta$  is indeed recorded along the axis of the eddy (Fig. 7), with bands of opposite  $\delta$  on each side. It is therefore possible that NIOs contribute to the observed pattern, even though we cannot verify whether or not the sign and the time dependence recorded by the drifters are indeed consistent with NIOs fluctuations. Similarly, NIOs could also contribute to the observed patterns in the submesoscale eddies on 26 and  
390 28 February (Figs. 8, 9).

## 6 Summary and Discussion

The surface evolution of a splitting eddy under windy conditions has been studied using drifter clusters that provide estimates of KPs, hydrographic sections, and reanalysis wind data during the period 23 – 28 February 2022. Surface drifters with drogues centered in the first meter, CARTHE and CODE, together provide a detailed look initially at the flank of the original eddy, then  
395 at the elongated eddy, and finally at the constellation of smaller eddies after the splitting. SVP drifters drogued at 15 m are more sparse but confirm that the flow is consistent within the surface layer and, importantly, allow a direct computation of vertical velocity  $w$  when co-located with the surface drifters.

The patterns in the observed KPs are interpreted in the context of the subsurface analysis of the same event based on smoothed Eulerian hydrographic profiles and an idealized unforced model presented by M24. The drifter-derived vorticity  
400 clearly delineates the eddy edge and reflects the intensification during the elongation process, as well as the separated eddy



centers following the splitting. This is consistent with the subsurface evolution. While M24's model results showed that external strain is not necessary for eddy splitting to occur, the drifters confirm a high strain rate during the elongation phase, which subsides following the splitting. The overall consistency between the two analyses suggests that the main processes acting on the surface are similar to those at depth. That is, the internal dynamics highlighted by M24 also appear to dominate the surface evolution, although the drifters also suggest a possible contribution of large-scale strain rate in the initial eddy elongation.

Possibly most interesting — but also most challenging to interpret — are the divergence patterns. The drifter data show high spatial variability of divergence throughout the time period, due to the strong influence of submesoscale processes on this KP. At the scale of the eddy, cyclogeostrophic balance (as proposed as leading splitting mechanism by M24) suggests a quadrupole pattern of alternating positive-negative-positive-negative divergence in the four quadrants of the eddy. At the surface, this is modified by the substantial winds on 25 and especially 26 February.

As we do not have drifter data around the full eddy perimeter, the quadrupole pattern cannot be directly verified. The theory (and M24 model) predict regions of positive divergence at the downstream side of the narrow end of an elliptical eddy, which is where the drifters are located on 23 February. Indeed, we observe predominantly positive divergence. However, there are also bands of negative divergence, both inside the eddy and on the outer edge. Later, during the elongation on 25 February and the splitting on 26 February, the overall divergence patterns are consistent with upwelling (positive divergence) inside the eddy, as the isopycnals dome, followed by downwelling (negative divergence) as the isopycnals flatten and the eddy splits. On 28 February, as new doming of the isopycnals can be detected in the hydrography, the divergence reflects this with mostly positive values near the center of the newly formed submesoscale eddy.

These differences in the divergence field between the quadrupole structure predicted by the unforced idealized model in M24 and the observed striated patterns may be partially explained as due to wind effects in the surface layer. Nonlinear Ekman pumping velocity  $w_{E_{knl}}$  is estimated from wind data and  $\zeta$  estimates, establishing the expected tendency of the surface flow, even though the high variability of the wind likely prevents its full realization. The analysis shows that the main contribution of Ekman pumping to the observed  $w$  pattern is in the form of a dipole, causing alternating downwelling and upwelling on the two sides of the cyclone, depending on wind direction. The expected  $w_{E_{knl}}$  patterns are compatible with the  $w$  and divergence estimates from drifter observations, where these are available. In addition,  $w_{E_{knl}}$  is roughly of the same order of magnitude as the full  $w$ , indicating that wind effects on the observed surface divergence and vertical velocity are not negligible. Overall,  $w$  was found to exhibit higher values (both negative and positive) than  $w_{E_{knl}}$ , which is to be expected, both because other processes contribute to the vertical velocity and because wind data are smoothed over much larger scales than the drifter observations, resulting in the smoothing of the  $w_{E_{knl}}$  estimates.

In addition to Ekman pumping, wind effects on divergence also include higher frequency processes such as NIOs. While a quantitative estimate of these effects is not possible, the observed vorticity and divergence patterns are consistent with an NIO contribution. Also, wind effects are likely to modify turbulent processes in the surface layer, therefore impacting the possible generation of submesoscales through the transient turbulent thermal wind balance (Dauhajre and McWilliams, 2018).

The 2022 CALYPSO experiment yielded a rich observational dataset, specifically and fortuitously targeting a mesoscale eddy about to split into several submesoscale eddies, thereby providing an unusually detailed picture of the evolution. Yet,



the resulting description provides only a partial 4D picture of the processes in action. M24 managed to achieve remarkable subsurface coverage through smoothing and interpolation; here we added the surface description, with special attention to the impact of the strong wind events that happened during the eddy splitting. A full accounting of the different processes, both steady and transient, however, remains out of reach. Describing all the facets and their interactions may well require  
440 further modeling work. Nevertheless, the present analysis definitively shows that cyclogeostrophic instabilities leading to eddy splitting are modified in the present case by strong shear and winds. Moreover, the vertical transport induced by the nonlinear interaction of the wind with the cyclone is a significant component of the total vertical exchange associated with the edges of the eddy. Other wind effects are likely to contribute to the high spatial variability of the divergence patterns observed by the drifters.

445 *Data availability.* ERA5 wind data are available from the Copernicus Climate Change Service at <https://cds.climate.copernicus.eu/cdsapp#!/dataset/reanalysis-era5-single-levels>. The observations collected during the CALYPSO experiment are available upon request.

*Author contributions.* MB and AG conceived the study; SD and HSH contributed the formal analysis and visualization; MB, SD, AG, HSH, and LM performed the interpretation; AG wrote the initial draft with contributions from HSH, MB, and SD; LC, TO, and PP provided drifter data; all authors reviewed the draft.

450 *Competing interests.* All authors declare no competing interests

*Acknowledgements.* Support for this work was provided by the US Office of Naval Research Coherent Lagrangian Pathways from the Surface Ocean to the Interior (CALYPSO) project (grant numbers N00014-22-1-2039, N00014-18-1-2461, and N00014-20-1-2754), as well as by Eurofleets+ in the form of ship time for the CALYPSO cruise. We thank the crews of both the R/V Pourquoi Pas? and the R/V Pelagia for their support of the CALYPSO experiment, especially Tom Farrar and his group for providing the ecoCTD data. We are also grateful to  
455 Amala Mahadevan for insightful conversations on this topic.



## References

- Amores, A., Jordà, G., Arsouze, T., and Le Sommer, J.: Up to what extent can we characterize ocean eddies using present-day gridded altimetric products?, *J. Geophys. Res. Oceans*, 123, 7220–7236, <https://doi.org/10.1029/2018JC014140>, 2018.
- Arai, M. and Yamagata, T.: Asymmetric evolution of eddies in rotating shallow water, *Chaos*, 4, 163–175, <https://doi.org/10.1063/1.166001>,  
460 1994.
- Asselin, O. and Young, W. R.: Penetration of Wind-Generated Near-Inertial Waves into a Turbulent Ocean, *Journal of Physical Oceanography*, 50, 1699 – 1716, <https://doi.org/10.1175/JPO-D-19-0319.1>, 2020.
- Berta, M., Griffa, A., Magaldi, M. G., Özgökmen, T. M., Poje, A. C., Haza, A. C., and Olascoaga, M. J.: Improved Surface Velocity and Trajectory Estimates in the Gulf of Mexico from Blended Satellite Altimetry and Drifter Data, *J. Atmos. Oceanic Technol.*, 32, 1880–1901,  
465 <https://doi.org/10.1175/JTECH-D-14-00226.1>, 2015.
- Berta, M., Bellomo, L., Griffa, A., Magaldi, M. G., Molcard, A., Mantovani, C., Gasparini, G. P., Marmain, J., Vetrano, A., Béquery, L., Borghini, M., Barbin, Y., Gaggelli, J., and Quentin, C.: Wind-induced variability in the Northern Current (northwestern Mediterranean Sea) as depicted by a multi-platform observing system, *Ocean Science*, 14, 689–710, <https://doi.org/10.5194/os-14-689-2018>, 2018.
- Berta, M., Griffa, A., Haza, A. C., Horstmann, J., Huntley, H. S., Ibrahim, R., Lund, B., Özgökmen, T. M., and Poje, A. C.: Subme-  
470 soscale Kinematic Properties in Summer and Winter Surface Flows in the Northern Gulf of Mexico, *J. Geophys. Res. Oceans*, 125, e2020JC016085, <https://doi.org/10.1029/2020JC016085>, 2020.
- Cao, H., Freilich, M. A., Song, X., Jing, Z., Fox-Kemper, B., Qiu, B., Hetland, R. D., Chai, F., Ruiz, S., and Chen, D.: Isopycnal Submesoscale Stirring Crucially Sustaining Subsurface Chlorophyll Maximum in Ocean Cyclonic Eddies, *Geophys. Res. Lett.*, 51, e2023GL105793, <https://doi.org/10.1029/2023GL105793>, 2024.
- 475 Centurioni, L. R.: Drifter Technology and Impacts for Sea Surface Temperature, Sea-Level Pressure, and Ocean Circulation Studies, in: *Observing the Oceans in Real Time*, edited by Venkatesan, R., Tandon, A., D’Asaro, E. A., and Atmanand, M. A., pp. 37–57, Springer, [https://doi.org/10.1007/978-3-319-66493-4\\_3](https://doi.org/10.1007/978-3-319-66493-4_3), 2018.
- Chelton, D. B., Schlax, M. G., and Samelson, R. M.: Global observations of nonlinear mesoscale eddies, *Prog. Oceanogr.*, 91, 167–216, <https://doi.org/10.1016/j.pocean.2011.01.002>, 2011.
- 480 Chen, Y., Straub, D., and Nadeau, L.-P.: Interaction of Nonlinear Ekman Pumping, Near-Inertial Oscillations, and Geostrophic Turbulence in an Idealized Coupled Model, *Journal of Physical Oceanography*, 51, 975 – 987, <https://doi.org/10.1175/JPO-D-20-0268.1>, 2021.
- CMEMS: Mediterranean Sea, Bio-Geo-Chemical, L3, daily Satellite Observations (1997-ongoing), <https://doi.org/10.48670/moi-00299>, 2022.
- Cushman-Roisin, B. and Beckers, J.-M.: *Introduction to Geophysical Fluid Dynamics: Physical and Numerical Aspects*, International geophysics series ; v. 101, Academic Press, Waltham, Mass, 2nd ed. edn., ISBN 1-283-27593-7, 2011.
- 485 D’Asaro, E. A., Shcherbina, A. Y., Klymak, J. M., Molemaker, M. J., Novelli, G., Guigand, C. M., Haza, A. C., Haus, B. K., Ryan, E. H., Jacobs, G. A., Huntley, H. S., Laxague, N. J. M., Chen, S., Judt, F., McWilliams, J. C., Barkan, R., Kirwan Jr., A. D., Poje, A. C., and Özgökmen, T. M.: Ocean convergence and the dispersion of flotsam, *Proc. Natl. Acad. Sci. USA*, 115, 1162–1167, <https://doi.org/10.1073/pnas.1718453115>, 2018.
- 490 Dauhajre, D. P. and McWilliams, J. C.: Diurnal Evolution of Submesoscale Front and Filament Circulations, *Journal of Physical Oceanography*, 48, 2343 – 2361, <https://doi.org/10.1175/JPO-D-18-0143.1>, 2018.





- Davis, R. E.: Drifter observations of coastal surface currents during CODE: The method and descriptive view, *J. Geophys. Res. Oceans*, 90, 4741–4755, <https://doi.org/10.1029/JC090iC03p04741>, 1985.
- Dever, M., Freilich, M. A., Farrar, J. T., Hodges, B., Lanagan, T., Baron, A. J., and Mahadevan, A.: EcoCTD for Profiling Oceanic Physical-  
495 Biological Properties from an Underway Ship, *J. Atmos. Oceanic Technol.*, 37, 825–840, <https://doi.org/10.1175/JTECH-D-19-0145.1>, 2020.
- Dewar, W. K. and Flierl, G. R.: Some Effects of the Wind on Rings, *Journal of Physical Oceanography*, 17, 1653 – 1667, [https://doi.org/10.1175/1520-0485\(1987\)017<1653:SEOTWO>2.0.CO;2](https://doi.org/10.1175/1520-0485(1987)017<1653:SEOTWO>2.0.CO;2), 1987.
- Elipot, S., Lumpkin, R., and Prieto, G.: Modification of inertial oscillations by the mesoscale eddy field, *Journal of Geophysical Research: Oceans*, 115, <https://doi.org/https://doi.org/10.1029/2009JC005679>, 2010.  
500
- Escudier, R., Renault, L., Pascual, A., Brasseur, P., Chelton, D., and Beuvier, J.: Eddy properties in the Western Mediterranean Sea from satellite altimetry and a numerical simulation, *J. Geophys. Res. Oceans*, 121, 3990–4006, <https://doi.org/10.1002/2015JC011371>, 2016.
- Esposito, G., Berta, M., Centurioni, L., Johnston, T. S., Lodise, J., Özgökmen, T., Poulain, P.-M., and Griffa, A.: Submesoscale Vorticity and Divergence in the Alboran Sea: Scale and Depth Dependence, *Frontiers in Marine Science*, 8, <https://doi.org/10.3389/fmars.2021.678304>,  
505 2021.
- Esposito, G., Donnet, S., Berta, M., Shcherbina, A. Y., Freilich, M., Centurioni, L., D’Asaro, E. A., Farrar, J. T., Johnston, T. M. S., Mahadevan, A., Özgökmen, T., Pascual, A., Poulain, P.-M., Ruiz, S., Tarry, D. R., and Griffa, A.: Inertial Oscillations and Frontal Processes in an Alboran Sea Jet: Effects on Divergence and Vertical Transport, *Journal of Geophysical Research: Oceans*, 128, e2022JC019004, <https://doi.org/https://doi.org/10.1029/2022JC019004>, 2023.
- 510 Essink, S., Hormann, V., Centurioni, L. R., and Mahadevan, A.: On Characterizing Ocean Kinematics from Surface Drifters, *J. Atmos. Oceanic Technol.*, 39, 1183–1198, <https://doi.org/10.1175/JTECH-D-21-0068.1>, 2022.
- Fu, L.-L., Chelton, D. B., Le Traon, P.-Y., and Morrow, R.: Eddy Dynamics from Satellite Altimetry, *Oceanography*, 23, 14–25, <https://doi.org/10.5670/oceanog.2010.02>, 2015.
- Gaube, P., Chelton, D. B., Samelson, R. M., Schlax, M. G., and O’Neill, L. W.: Satellite Observations of Mesoscale Eddy-Induced Ekman  
515 Pumping, *Journal of Physical Oceanography*, 45, 104 – 132, <https://doi.org/10.1175/JPO-D-14-0032.1>, 2015.
- Gonçalves, R. C., Iskandarani, M., Özgökmen, T. M., and Thacker, W. C.: Reconstruction of Submesoscale Velocity Field from Surface Drifters, *J. Phys. Oceanogr.*, 49, 941–958, <https://doi.org/10.1175/JPO-D-18-0025.1>, 2019.
- Graves, L. P., McWilliams, J. C., and Montgomery, M. T.: Vortex evolution due to straining: a mechanism for dominance of strong, interior anticyclones, *Geophys. Astrophys. Fluid Dynam.*, 100, 151–183, <https://doi.org/10.1080/03091920600792041>, 2006.
- 520 Hart, J. E.: A note on nonlinear corrections to the Ekman layer pumping velocity, *Physics of Fluids*, 12, 131–135, <https://doi.org/10.1063/1.870300>, 2000.
- Hersbach, H., Bell, B., Berrisford, P., Biavati, G., Horányi, A., Muñoz Sabater, J., Nicolas, J., Peubey, C., Radu, R., Rozum, I., Schepers, D., Simmons, A., Soci, C., Dee, D., and Thépaut, J.-N.: ERA5 hourly data on single levels from 1940 to present, <https://doi.org/10.24381/cds.adbb2d47>, 2023.
- 525 Huntley, H. S., Berta, M., Esposito, G., Griffa, A., Mourre, B., and Centurioni, L. R.: Conditions for Reliable Divergence Estimates from Drifter Triplets, *J. Atmos. Oceanic Technol.*, 39, 1499–1523, <https://doi.org/10.1175/JTECH-D-21-0161.1>, 2022.
- Johnson, H. K.: Simple expressions for correcting wind speed data for elevation, *Coastal Eng.*, 36, 263–269, [https://doi.org/10.1016/S0378-3839\(99\)00016-2](https://doi.org/10.1016/S0378-3839(99)00016-2), 1999.



- Kawai, H.: Scale dependence of divergence and vorticity of near-surface flows in the sea. Part 1. Measurements and calculations of area-averaged divergence and vorticity, *J. Oceanogr. Soc. Jpn.*, 41, 157–166, <https://doi.org/10.1007/BF02109190>, 1985.
- Kirincich, A. R. and Barth, J. A.: Time-Varying Across-Shelf Ekman Transport and Vertical Eddy Viscosity on the Inner Shelf, *Journal of Physical Oceanography*, 39, 602 – 620, <https://doi.org/10.1175/2008JPO3969.1>, 2009.
- Kunze, E.: Near-Inertial Wave Propagation In Geostrophic Shear, *Journal of Physical Oceanography*, 15, 544 – 565, [https://doi.org/10.1175/1520-0485\(1985\)015<0544:NIWPIG>2.0.CO;2](https://doi.org/10.1175/1520-0485(1985)015<0544:NIWPIG>2.0.CO;2), 1985.
- 535 Lodise, J., Özgökmen, T. M., Gonçalves, R. C., Iskandarani, M., Lund, B., Horstmann, J., Poulain, P.-M., Klymak, J., Ryan, E. H., and Guigand, C.: Investigating the Formation of Submesoscale Structures along Mesoscale Fronts and Estimating Kinematic Quantities Using Lagrangian Drifters, *Fluids*, 5, 159, <https://doi.org/10.3390/fluids5030159>, 2020.
- Lumpkin, R. and Pazos, M.: Measuring surface currents with Surface Velocity Program drifters: the instrument, its data, and some recent results, in: *Lagrangian Analysis and Prediction of Coastal and Ocean Dynamics*, edited by Griffa, A., Kirwan Jr., A. D., Mariano, A. J., Özgökmen, T. M., and Rossby, H. T., pp. 39–67, Cambridge University Press, <https://doi.org/10.1017/CBO9780511535901.003>, 2007.
- 540 Mahadevan, A. and D’Asaro, E. A.: Calypso 2022 Pourquoi Pas? Cruise Report, Tech. rep., Woods Hole Oceanographic Institute, <http://mseas.mit.edu/?p=6888>, 2024.
- Mahadevan, A., Thomas, L. N., and Tandon, A.: Comment on "Eddy/Wind Interactions Stimulate Extraordinary Mid-Ocean Plankton Blooms", *Science*, 320, 448–448, <https://doi.org/10.1126/science.1152111>, 2008.
- 545 Mahadevan, A., Pascual, A., Rudnick, D. L., Ruiz, S., Tintoré, J., and D’Asaro, E. A.: Coherent pathways for vertical transport from the surface ocean to interior, *Bull. Am. Meteorol. Soc.*, 101, E1996–E2004, <https://doi.org/10.1175/BAMS-D-19-0305.1>, 2020.
- Martínez-Moreno, J., Hogg, A. M., England, M. H., Constantinou, N. C., Kiss, A. E., and Morrison, A. K.: Global changes in oceanic mesoscale currents over the satellite altimetry record, *Nature Climate Change*, 11, 397–403, <https://doi.org/10.1038/s41558-021-01006-9>, 2021.
- 550 McGillicuddy, D. J., Anderson, L. A., Bates, N. R., Bibby, T., Buesseler, K. O., Carlson, C. A., Davis, C. S., Ewart, C., Falkowski, P. G., Goldthwait, S. A., Hansell, D. A., Jenkins, W. J., Johnson, R., Kosnyrev, V. K., Ledwell, J. R., Li, Q. P., Siegel, D. A., and Steinberg, D. K.: Eddy/Wind Interactions Stimulate Extraordinary Mid-Ocean Plankton Blooms, *Science*, 316, 1021–1026, <https://doi.org/10.1126/science.1136256>, 2007.
- McWilliams, J. C.: Submesoscale, coherent vortices in the ocean, *Rev Geophys*, 23, 165–182, <https://doi.org/10.1029/RG023i002p00165>, 555 1985.
- McWilliams, J. C.: A survey of submesoscale currents, *Geoscience Letters*, 6, <https://doi.org/10.1186/s40562-019-0133-3>, 2019.
- Menna, M., Gerin, R., Bussani, A., and Poulain, P.-M.: The OGS Mediterranean Drifter Dataset: 1986-2016, Tech. Rep. Rel. 2017/92 Sez. OCE 28 MAOS, OGS, Trieste, Italy, [http://argo.ogs.it/pub/Menna%20et%20al%202017\\_Drifter\\_database.pdf](http://argo.ogs.it/pub/Menna%20et%20al%202017_Drifter_database.pdf), 2017.
- Middleton, L., Wu, W., Johnston, T. M. S., Tarry, D. R., Farrar, J. T., Poulain, P.-M., Özgökmen, T. M., Shcherbina, A. Y., Pascual, A., 560 McNeill, C. L., Belgacem, M., Berta, M., Abbott, K., Worden, A. Z., Wittmers, F., Kinsella, A., Centurioni, L. R., Hormann, V., Cutolo, E., Tintoré, J., Ruiz, S., Casas, B., Cheslack, H., Collaboration, C., D’Asaro, E. A., and Mahadevan, A.: Cyclone splitting ventilates the upper ocean, submitted 2024.
- Mkhinini, N., Coimbra, A. L. S., Stegner, A., Arsouze, T., Taupier-Letage, I., and Béranger, K.: Long-lived mesoscale eddies in the eastern Mediterranean Sea: Analysis of 20 years of AVISO geostrophic velocities, *J. Geophys. Res. Oceans*, 119, 8603–8626, 565 <https://doi.org/10.1002/2014JC010176>, 2014.



- Molinari, R. and Kirwan Jr., A. D.: Calculations of Differential Kinematic Properties From Lagrangian Observations in the Western Caribbean Sea, *J. Phys. Oceanogr.*, 5, 483–491, [https://doi.org/10.1175/1520-0485\(1975\)005<0483:CODKPF>2.0.CO;2](https://doi.org/10.1175/1520-0485(1975)005<0483:CODKPF>2.0.CO;2), 1975.
- Munk, W., Armi, L., Fischer, K., and Zachariasen, F.: Spirals on the sea, *Proc. R. Soc. A*, 456, 1217–1280, <https://doi.org/10.1098/rspa.2000.0560>, 2000.
- 570 Niiler, P.: Chapter 4.1: The world ocean surface circulation, in: *Ocean Circulation and Climate*, edited by Siedler, G., Church, J., and Gould, J., pp. 193–204, Academic Press, [https://doi.org/10.1016/S0074-6142\(01\)80119-4](https://doi.org/10.1016/S0074-6142(01)80119-4), 2001.
- Niiler, P. P.: On the Ekman divergence in an oceanic jet, *Journal of Geophysical Research* (1896-1977), 74, 7048–7052, <https://doi.org/https://doi.org/10.1029/JC074i028p07048>, 1969.
- Niiler, P. P., Sybrandy, A. S., Bi, K., Poulain, P.-M., and Bitterman, D.: Measurements of the water-following capability of holey-sock and
- 575 TRISTAR drifters, *Deep-Sea Res Pt I*, 42, 1951–1964, [https://doi.org/10.1016/0967-0637\(95\)00076-3](https://doi.org/10.1016/0967-0637(95)00076-3), 1995.
- Nof, D.: The role of angular momentum in the splitting of isolated eddies, *Tellus*, 42A, 469–481, <https://doi.org/10.3402/tellusa.v42i4.11891>, 1990.
- Nof, D.: Fission of Single and Multiple Eddies, *J. Phys. Oceanogr.*, 21, 40–52, [https://doi.org/10.1175/1520-0485\(1991\)021<0040:FOSAME>2.0.CO;2](https://doi.org/10.1175/1520-0485(1991)021<0040:FOSAME>2.0.CO;2), 1991.
- 580 Novelli, G., Guigand, C. M., Cousin, C., Ryan, E. H., Laxague, N. J. M., Dai, H., Haus, B. K., and Özgökmen, T. M.: A Biodegradable Surface Drifter for Ocean Sampling on a Massive Scale, *J. Atmos. Oceanic Technol.*, 34, 2509–2532, <https://doi.org/10.1175/JTECH-D-17-0055.1>, 2017.
- Okubo, A., Ebbesmeyer, C. C., and Helseth, J. M.: Determination of Lagrangian deformations from analysis of current followers, *J. Phys. Oceanogr.*, 6, 524–527, [https://doi.org/10.1175/1520-0485\(1976\)006<0524:DOLDFA>2.0.CO;2](https://doi.org/10.1175/1520-0485(1976)006<0524:DOLDFA>2.0.CO;2), 1976.
- 585 Perkins, H.: Observed effect of an eddy on inertial oscillations, *Deep Sea Research and Oceanographic Abstracts*, 23, 1037–1042, [https://doi.org/https://doi.org/10.1016/0011-7471\(76\)90879-2](https://doi.org/https://doi.org/10.1016/0011-7471(76)90879-2), 1976.
- Petersen, M. R., Williams, S. J., Maltrud, M. E., Hecht, M. W., and Hamann, B.: A three-dimensional eddy census of a high-resolution global ocean simulation, *J. Geophys. Res. Oceans*, 118, 1759–1774, <https://doi.org/10.1002/jgrc.20155>, 2013.
- Pinot, J.-M., Tintoré, J., and Gomis, D.: Quasi-synoptic mesoscale variability in the Balearic Sea, *Deep Sea Research Part I: Oceanographic*
- 590 *Research Papers*, 41, 897–914, [https://doi.org/https://doi.org/10.1016/0967-0637\(94\)90082-5](https://doi.org/https://doi.org/10.1016/0967-0637(94)90082-5), 1994.
- Polvani, L. M., McWilliams, J. C., Spall, M. A., and Ford, R.: The coherent structures of shallow-water turbulence: Deformation-radius effects, cyclone/anticyclone asymmetry and gravity-wave generation, *Chaos*, 4, 177–186, <https://doi.org/10.1063/1.166002>, 1994.
- Poulain, P.-M.: Drifter observations of surface circulation in the Adriatic Sea between December 1994 and March 1996, *J. Mar. Syst.*, 20, 231–253, [https://doi.org/10.1016/S0924-7963\(98\)00084-0](https://doi.org/10.1016/S0924-7963(98)00084-0), 1999.
- 595 Poulain, P.-M., Centurioni, L. R., and Özgökmen, T. M.: Comparing the Currents Measured by CARTHE, CODE and SVP Drifters as a Function of Wind and Wave Conditions in the Southwestern Mediterranean Sea, *Sensors*, 22, 353, <https://doi.org/10.3390/s22010353>, 2022.
- Resplandy, L., Lévy, M., and McGillicuddy Jr., D. J.: Effects of Eddy-Driven Subduction on Ocean Biological Carbon Pump, *Global Biogeochemical Cycles*, 33, 1071–1084, <https://doi.org/https://doi.org/10.1029/2018GB006125>, 2019.
- 600 Ruiz, S., Pascual, A., Garau, B., Faugère, Y., Alvarez, A., and Tintoré, J.: Mesoscale dynamics of the Balearic Front, integrating glider, ship and satellite data, *Journal of Marine Systems*, 78, S3–S16, <https://doi.org/https://doi.org/10.1016/j.jmarsys.2009.01.007>, coastal Processes: Challenges for Monitoring and Prediction, 2009.
- Saucier, W. J.: *Principles of meteorological analysis*, vol. 438, University of Chicago Press, Chicago, IL, ISBN 0226735338, 1955.



- 605 Song, H., Marshall, J., McGillicuddy, D. J., and Seo, H.: Impact of Current-Wind Interaction on Vertical Processes in the Southern Ocean, *J. Geophys. Res. Oceans*, 125, e2020JC016046, <https://doi.org/10.1029/2020JC016046>, 2020.
- Stegner, A., Le Vu, B., Dumas, F., Ghannami, M. A., Nicolle, A., Durand, C., and Faugere, Y.: Cyclone-Anticyclone Asymmetry of Eddy Detection on Gridded Altimetry Product in the Mediterranean Sea, *J. Geophys. Res. Oceans*, 126, e2021JC017475, <https://doi.org/10.1029/2021JC017475>, 2021.
- 610 Stern, M. E.: Interaction of a uniform wind stress with a geostrophic vortex, *Deep Sea Res.*, 12, 355–367, [https://doi.org/10.1016/0011-7471\(65\)90007-0](https://doi.org/10.1016/0011-7471(65)90007-0), 1965.
- Tarry, D. R., Essink, S., Pascual, A., Ruiz, S., Poulain, P.-M., Özgökmen, T., Centurioni, L. R., Farrar, J. T., Shcherbina, A., Mahadevan, A., and D’Asaro, E.: Frontal Convergence and Vertical Velocity Measured by Drifters in the Alboran Sea, *Journal of Geophysical Research: Oceans*, 126, e2020JC016614, <https://doi.org/https://doi.org/10.1029/2020JC016614>, e2020JC016614 2020JC016614, 2021.
- 615 Tarry, D. R., Ruiz, S., Johnston, T. M. S., Poulain, P.-M., Özgökmen, T. M., Centurioni, L. R., Berta, M., Esposito, G., Farrar, J. T., Mahadevan, A., and Pascual, A.: Drifter observations reveal intense vertical velocity in a surface ocean front, *Geophys. Res. Lett.*, 49, e2022GL098969, <https://doi.org/10.1029/2022GL098969>, 2022.
- Volpe, G., Colella, S., Brando, V. E., Forneris, V., La Padula, F., Di Cicco, A., Sammartino, M., Bracaglia, M., Artuso, F., and Santoleri, R.: Mediterranean ocean colour Level 3 operational multi-sensor processing, *Ocean Sci.*, 15, 127–146, <https://doi.org/10.5194/os-15-127-2019>, 2019.
- 620 Wenegrat, J. O. and Thomas, L. N.: Ekman Transport in Balanced Currents with Curvature, *J. Phys. Oceanogr.*, 47, 1189–1203, <https://doi.org/10.1175/JPO-D-16-0239.1>, 2017.

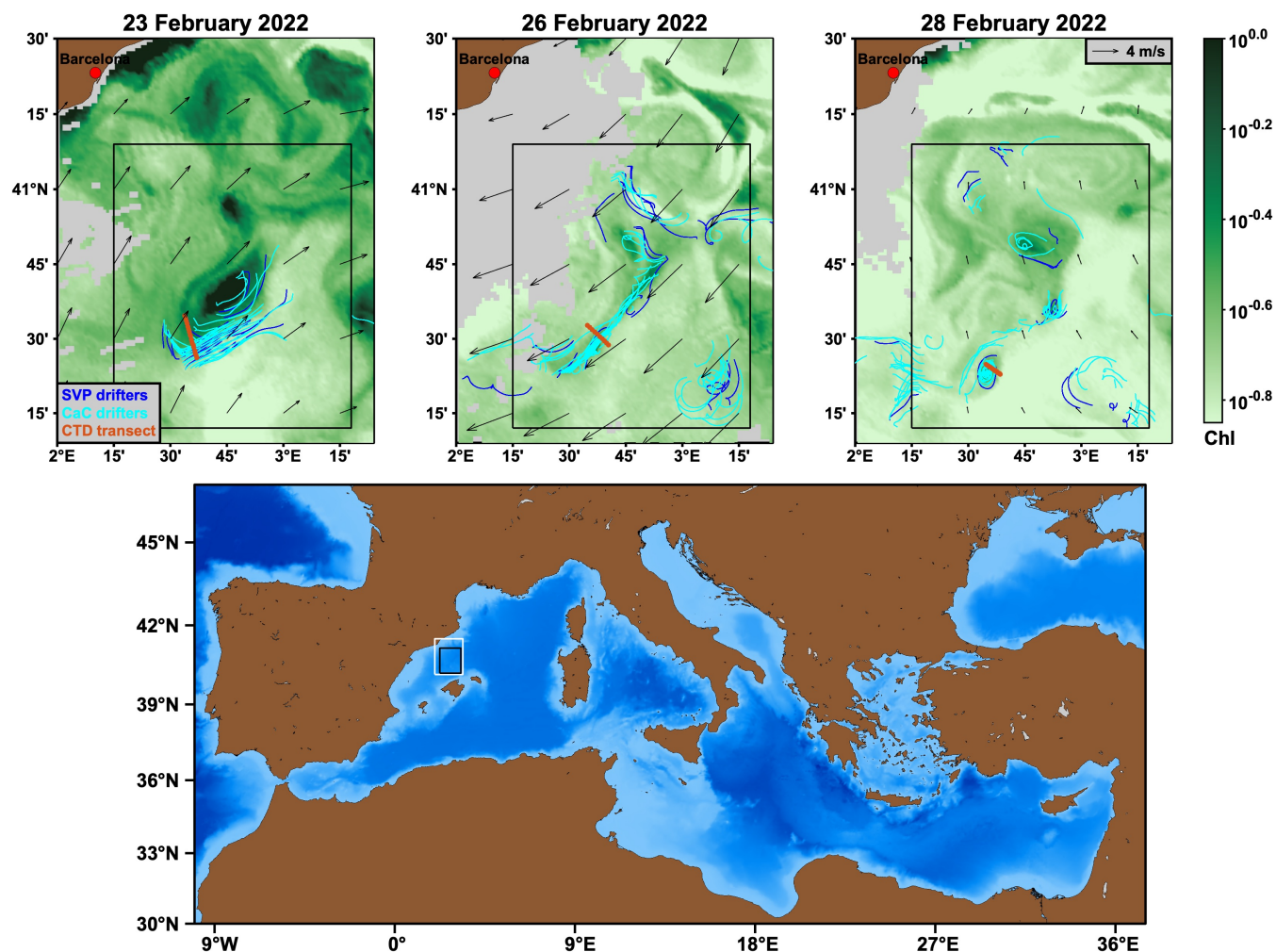


**Figure 1.** Top: Maps of the Balearic Sea with chlorophyll concentration from satellites (background color), wind (vectors), and in situ observations, with underway CTD sections in red and CARTHE/CODE and SVP drifter trajectories in cyan and blue, respectively, for (from left to right) 23 February, 26 February, and 28 February 2022. Bottom: Overview of the Mediterranean Sea, indicating the position of the top maps (white box). The black box in all frames shows the position of the geographic panels in Figure 5 and later.

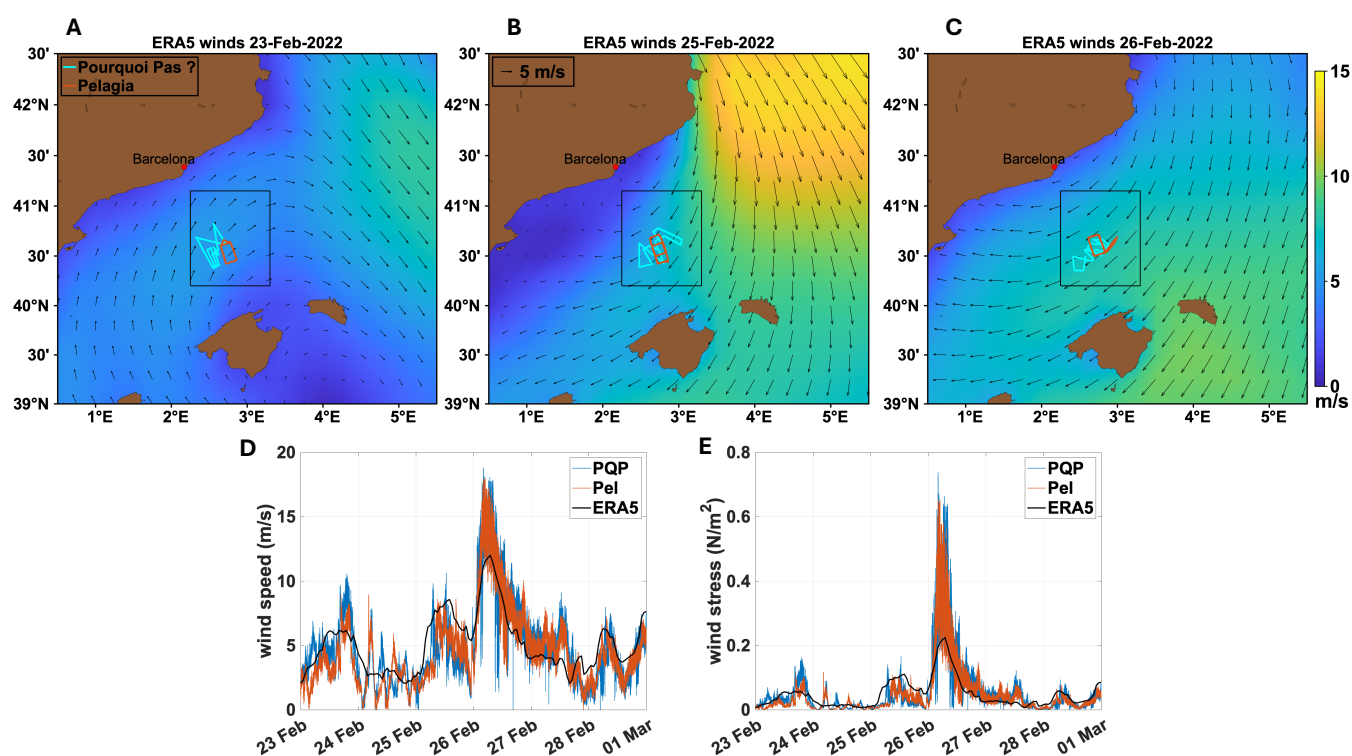


**Figure 2.** Top: Wind maps at 10 m from ERA5. The red (cyan) path shows the R/V Pelagia (R/V Pourquoi Pas?) ship track on the corresponding dates (February 23, 25, 26). The black square indicates the area over which the wind has been averaged to obtain the wind time series plotted in panel D) (wind speed) and E) (wind stress) together with in situ wind observations from the two oceanographic vessels involved in the CALYPSO 2022 experiment (R/V Pourquoi Pas? in blue and R/V Pelagia in red).



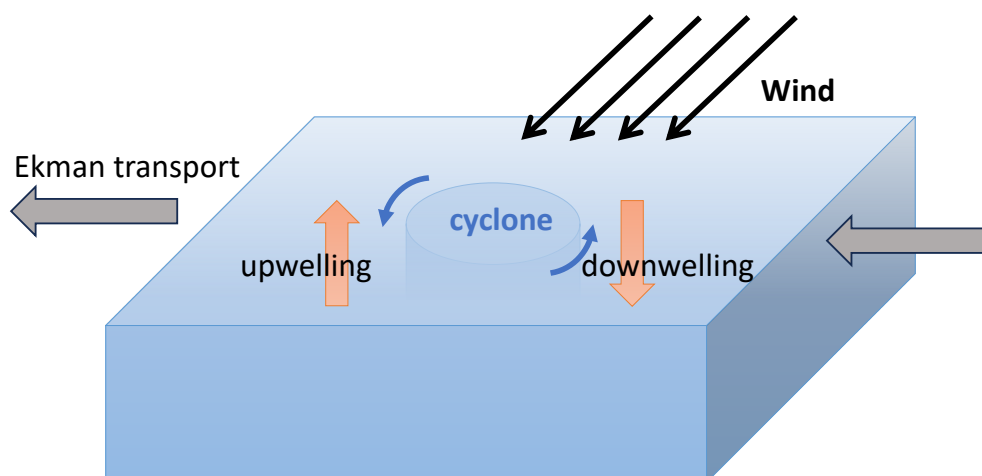


**Figure 3.** Schematic of wind-induced 3D transport on a marine cyclone.

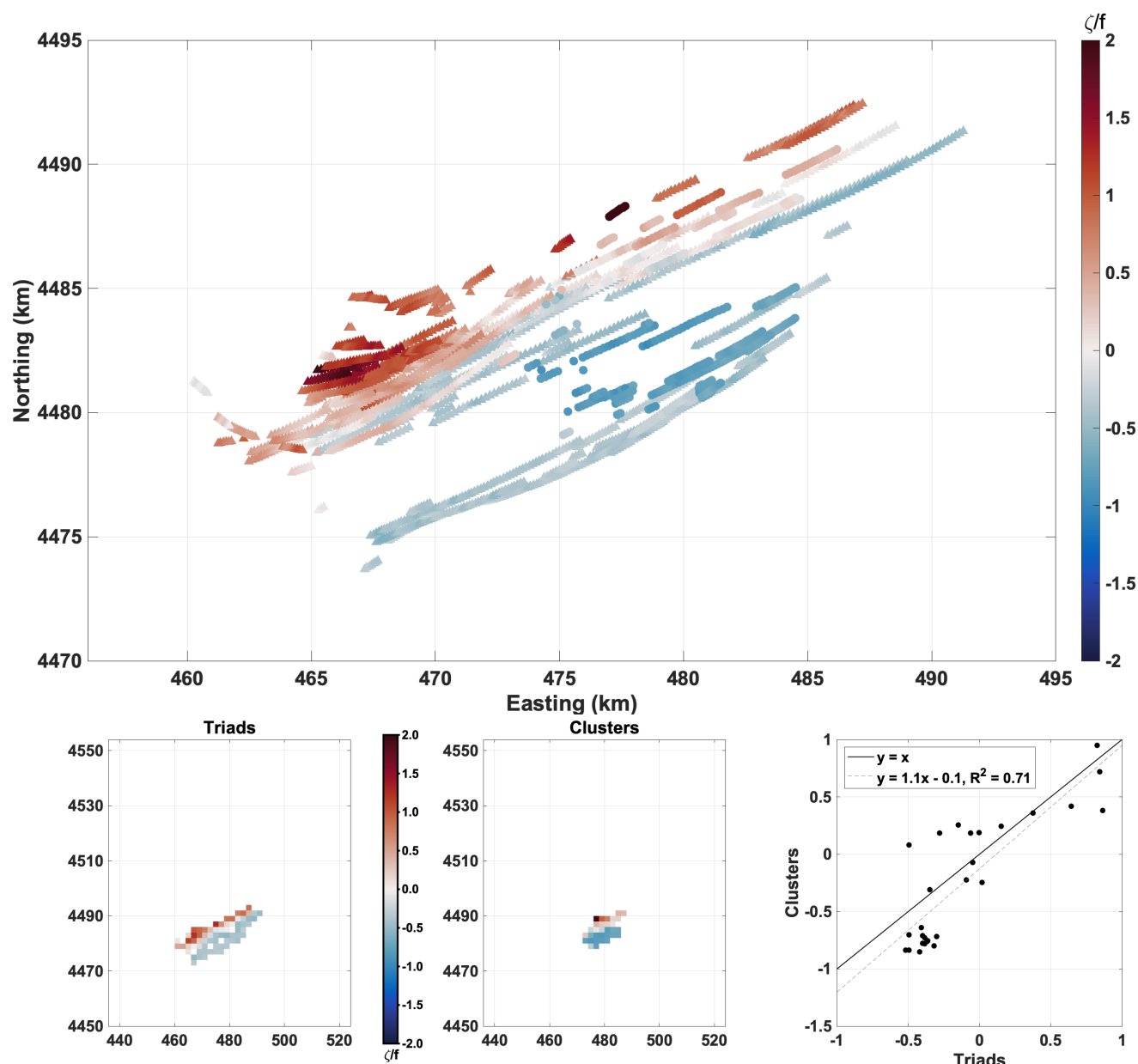


**Figure 4.** Comparison of normalized vorticity estimates from drifter triplets and clusters (2 – 4 km scale) as derived from CARTHE/CODE drifters, for 23 February 2022. Top: Individual estimates from drifter triplets (triangles) and clusters (dots). Bottom: Bin averages obtained from estimates with each method, left – triplets, center – clusters. Bottom right: Scatter plot relating the bin averages with least-squares fit (gray, dashed line) and one-to-one line (black, solid line).



## CARTHE/CODE, 23 February

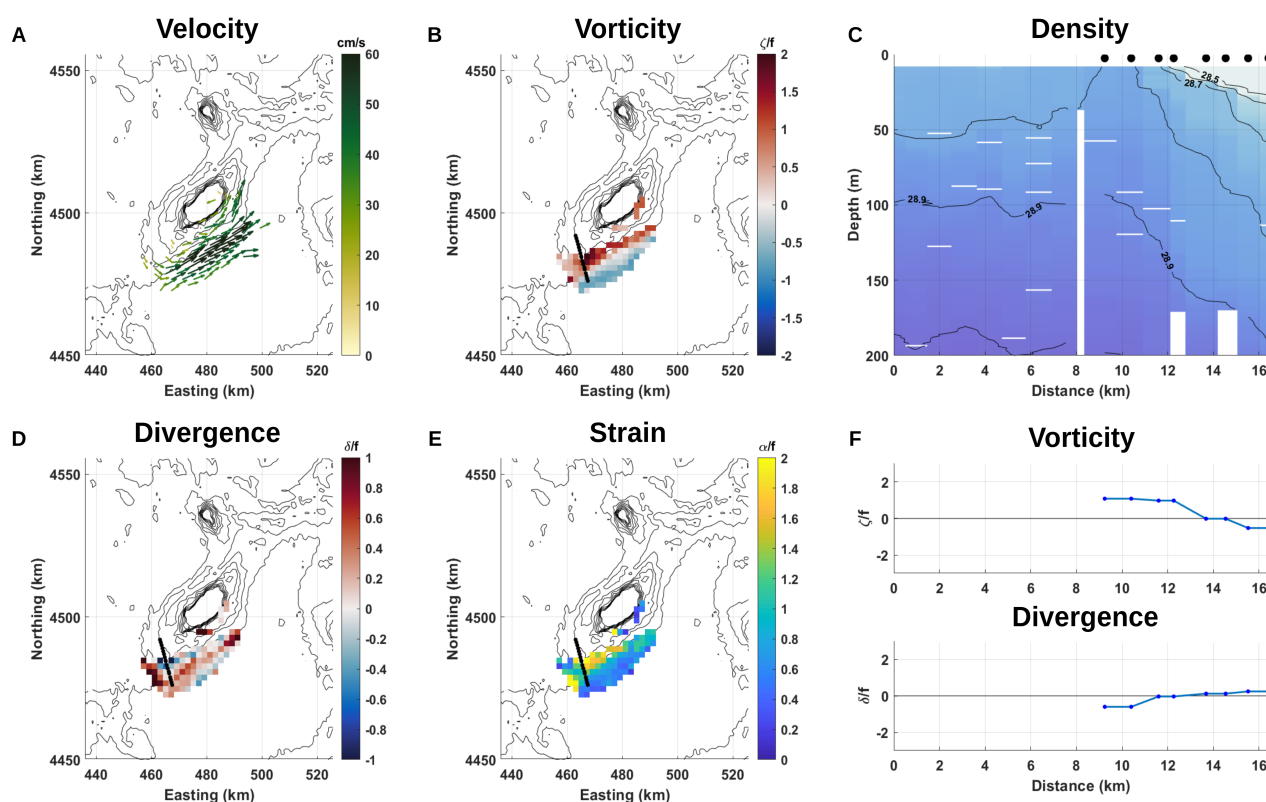


**Figure 5.** Surface and water column properties from in situ samplings in 23 February 2022: A) surface currents derived from CARTHE/CODE (1m depth) drifter trajectories. B,C,D) surface vorticity, divergence, and strain rate (normalized by local  $f$ ) as derived from CARTHE/CODE drifter triplets; black thin contours show chlorophyll isolines (see Figure 1). The black line indicates the location of the underway CTD potential density transect (kg/m<sup>3</sup>) shown in panel E). Panel F) shows the vorticity (upper panel) and divergence (lower panel) along the CTD transect.



## SVP, 23 February

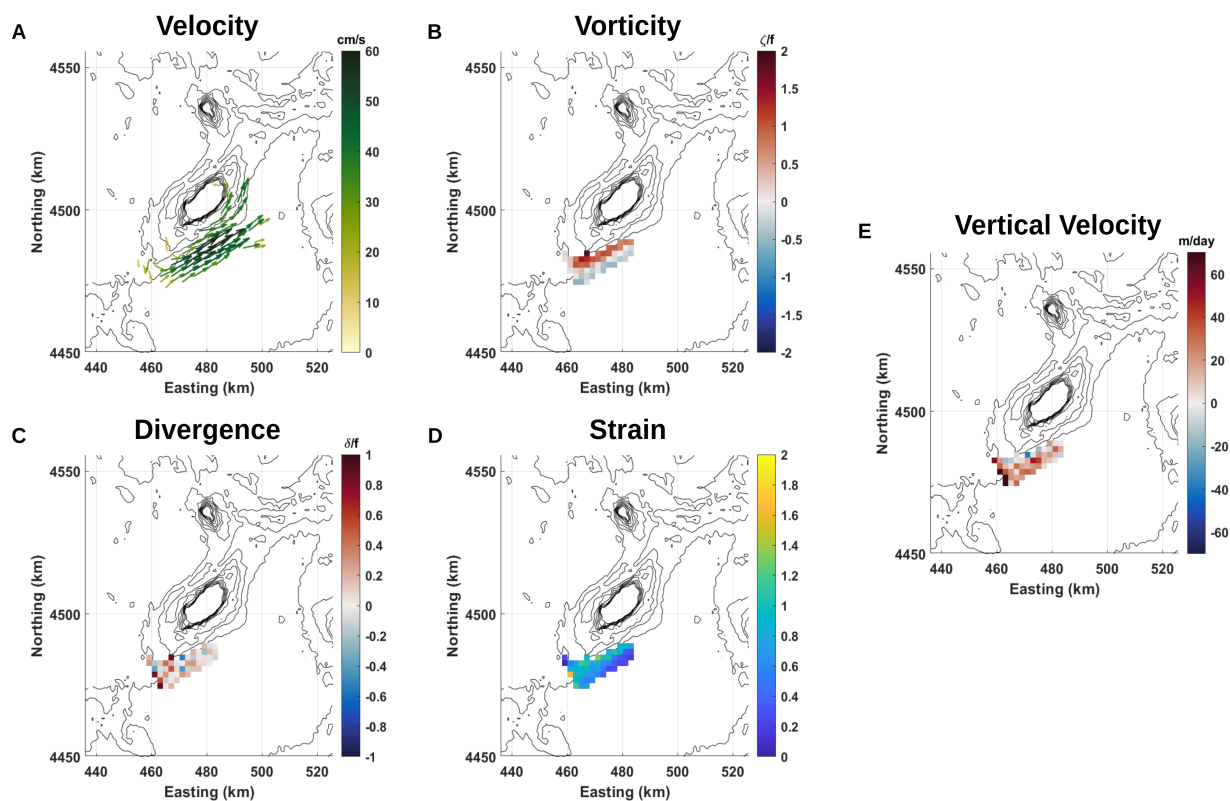


**Figure 6.** A) 15m-depth currents derived from SVP drifter trajectories for 23 February 2022. B,C,D) surface vorticity, divergence, and strain rate (normalized by local  $f$ ) as derived from SVP drifter triplets; black thin contours show chlorophyll isolines (see Figure 1). E) Vertical velocity within the first 15m depth layer, estimated through continuity equation from divergence at 1 m and 15 m depth.



## CARTHE/CODE, 25 February

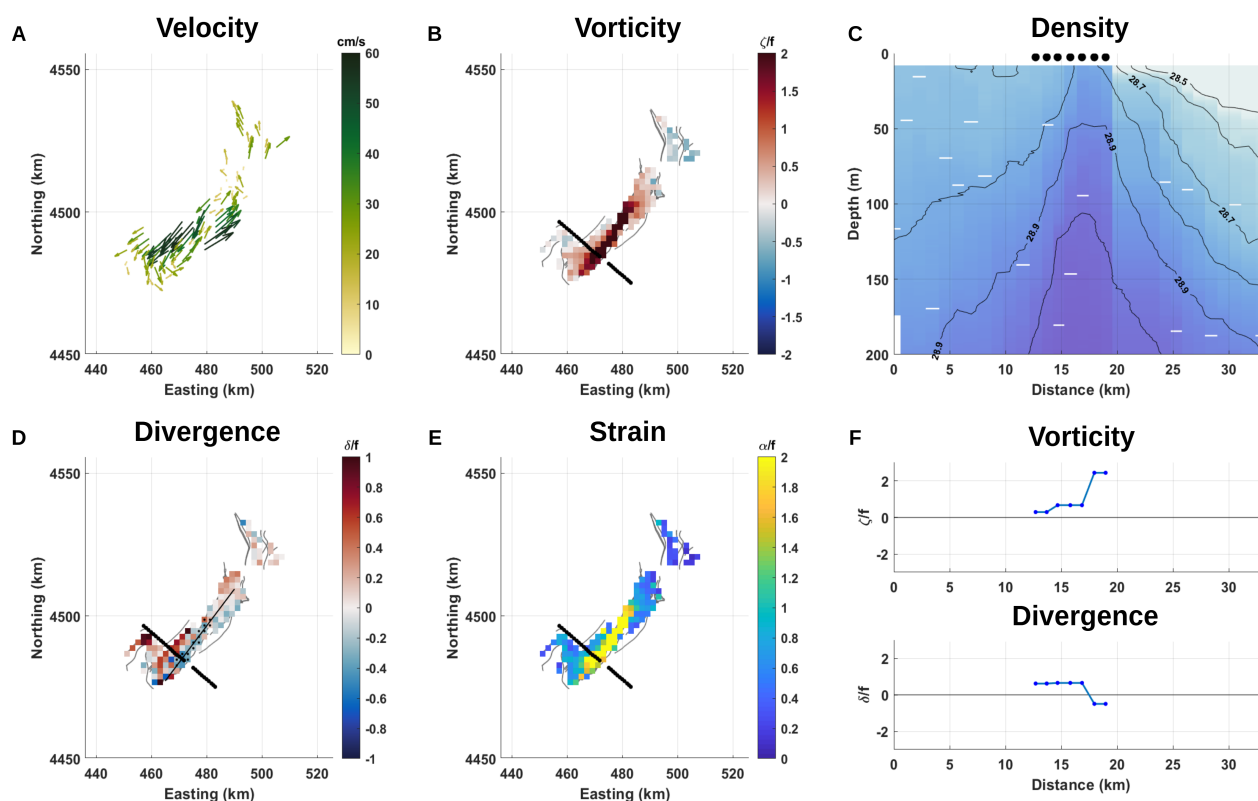


**Figure 7.** Same as Figure 5 but for 25 February 2022. Black thin contours show drifter trajectories (see Figure 1). Chlorophyll concentrations are not available for this date.



## CARTHE/CODE, 26 February

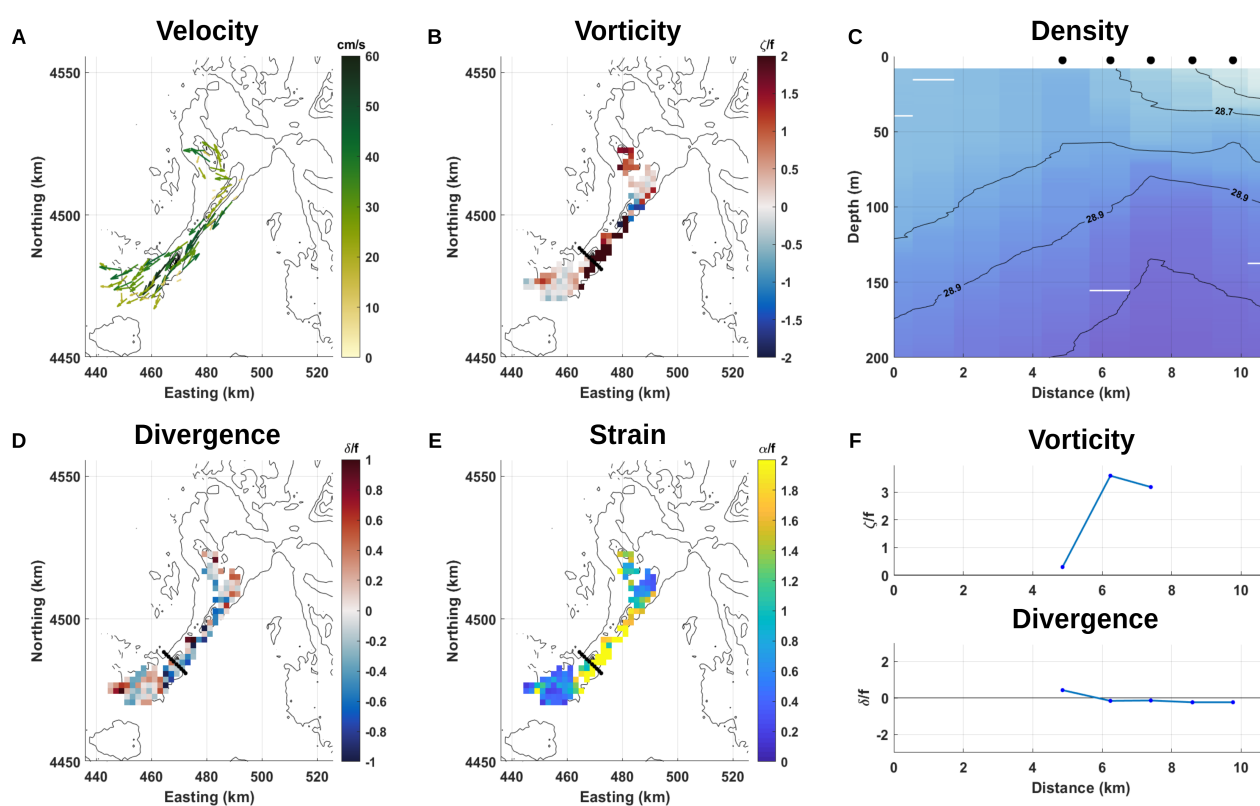


**Figure 8.** Same as Figure 5 but for 26 February 2022. (Please note the reduced bin coverage around the ecoCTD transect in panel B) compared to panel C) which explains the different length of the lines in panel F).





## CARTHE/CODE, 28 Febuary

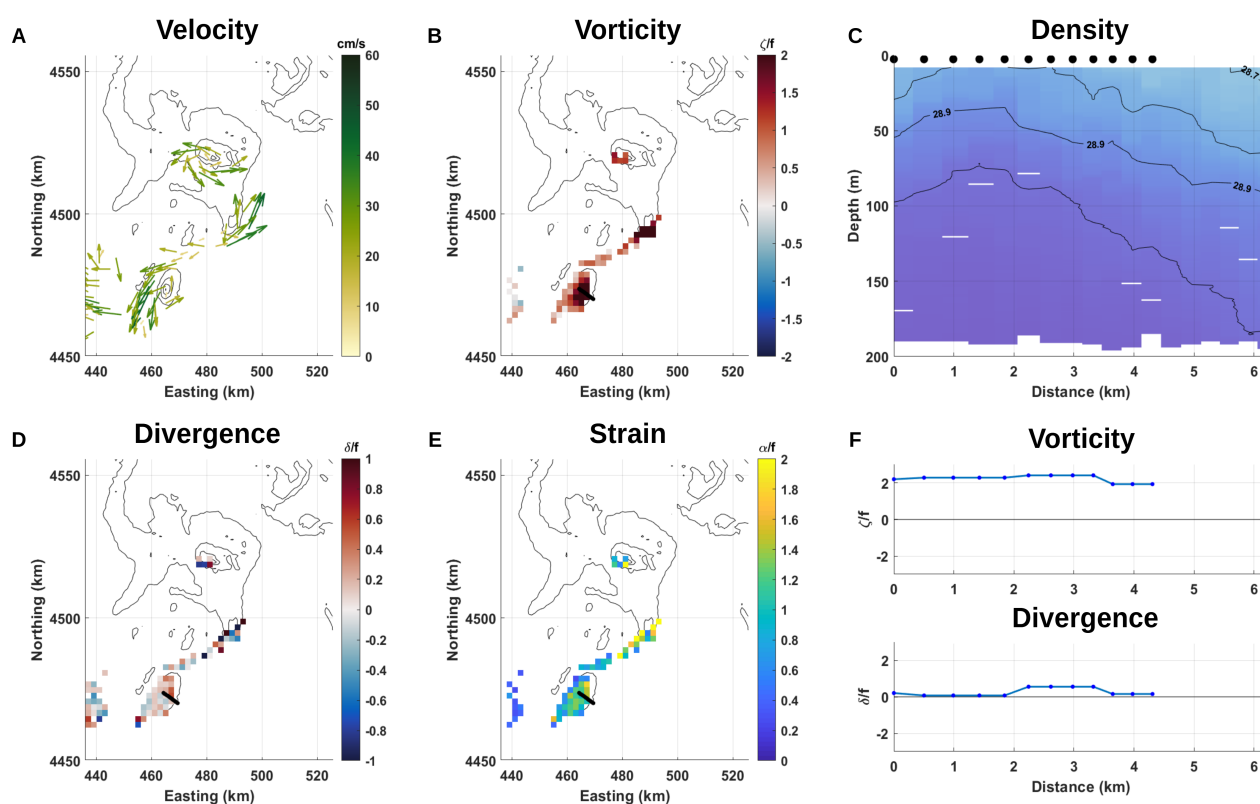


**Figure 9.** Same as Figure 5 but for 28 February 2022.



# Ekman transport and pumping velocity

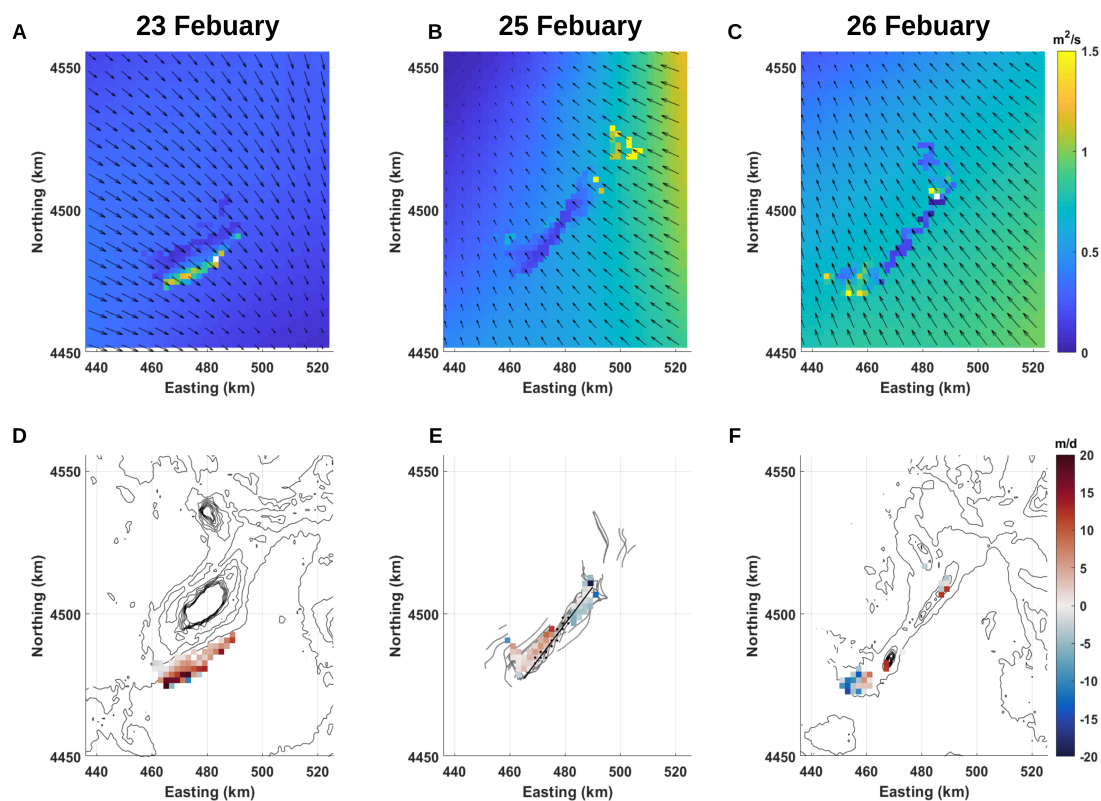


**Figure 10.** Top: Nonlinear Ekman transport magnitude and direction for (A) 23 February, (B) 25 February, and (C) 26 February as perturbed by surface vorticity estimated from drifter triplets coverage, superposed on the linear Ekman transport outside the drifter coverage. Bottom: Ekman pumping velocity derived from Ekman transport divergence for (D) 23 February, (E) 25 February, and (F) 26 February.

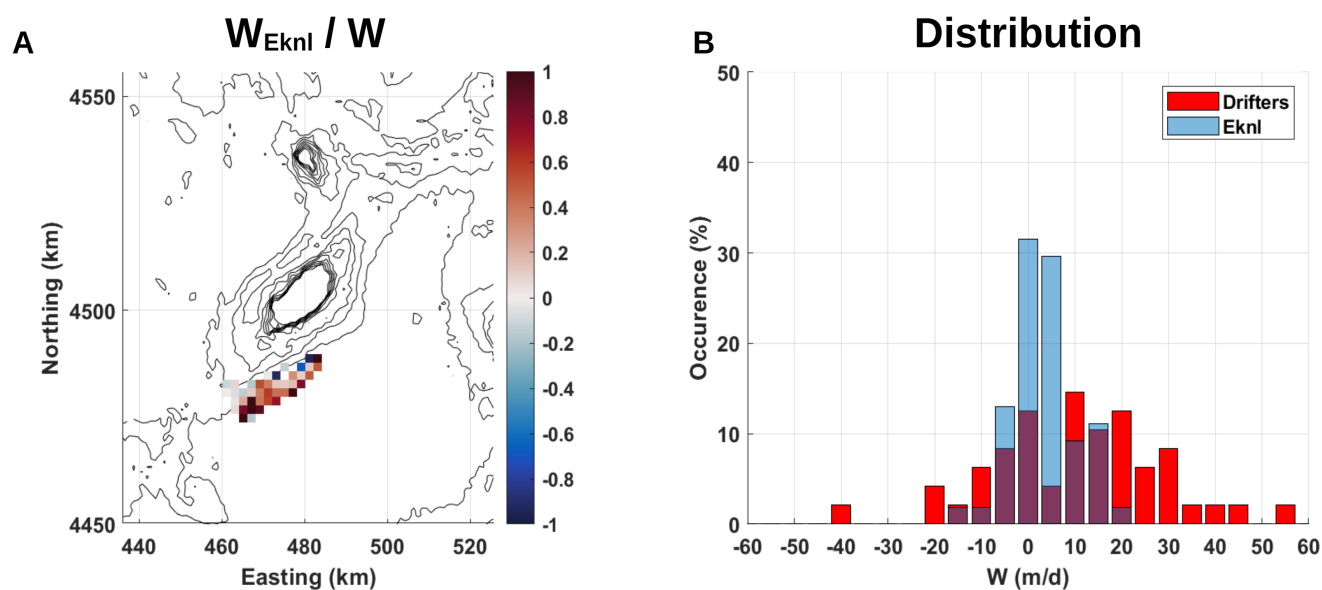


**Figure 11.** (A) Ratio of Ekman pumping to vertical velocity calculated from drifter divergence on 23 February. (B) Comparison of probability density functions for Ekman pumping estimates and for vertical velocity from drifters for 23 February.